RAA 2015 Vol. **15** No. **8**, 1294–1324 doi: 10.1088/1674–4527/15/8/014
http://www.raa-journal.org *http://www.iop.org/journals/raa*

***R**esearch in*
***A**stronomy and*
***A**strophysics*

Evolutionary stages and disk properties of young stellar objects in the Perseus cloud

Hong-Xin Zhang** [1,2,3,4,10], Yu Gao [5,6], Min Fang [5,7], Hai-Bo Yuan [3], Ying-He Zhao [5,6,8], Rui-Xiang Chang [9], Xue-Jian Jiang [5,6], Xiao-Wei Liu [3], A-Li Luo [1], Hong-Jun Ma [5,6], Zheng-Yi Shao [9] and Xiao-Long Wang [5,6]

[1] National Astronomical Observatories, Chinese Academy of Sciences, Beijing 100012, China
[2] Department of Astronomy, Peking University, Beijing 100871, China; *hongxin@pku.edu.cn*
[3] Kavli Institute for Astronomy and Astrophysics, Peking University, Beijing 100871, China
[4] Chinese Academy of Sciences South America Center for Astronomy, Camino EI Observatorio #1515, Las Condes, Santiago, Chile
[5] Purple Mountain Observatory, Chinese Academy of Sciences, Nanjing 210008, China; *yugao@pmo.ac.cn*
[6] Key Laboratory of Radio Astronomy, Chinese Academy of Sciences, Nanjing 210008, China
[7] Departamento de Física Teórica Universidad Autónoma de Madrid, 28049 Cantoblanco, Madrid, Spain; *mfang.cn@gmail.com*
[8] Infrared Processing and Analysis Center, California Institute of Technology, MS 100-22, Pasadena, CA 91125, USA
[9] Key Laboratory for Research in Galaxies and Cosmology, Shanghai Astronomical Observatory, Chinese Academy of Sciences, Shanghai 200030, China
[10] Instituto de Astrofísica, Facultad de Física, Pontificia Universidad Católica de Chile, Av. Vicuña Mackenna 4860, 7820436 Macul, Santiago, Chile

Received 2015 April 2; accepted 2015 June 1

Abstract We investigated the evolutionary stages and disk properties of 211 young stellar objects (YSOs) across the Perseus cloud by modeling their broadband optical to mid-infrared (IR) spectral energy distribution (SED). Our optical gri photometry data were obtained from the recently finished Purple Mountain Observatory Xuyi Schmidt Telescope Photometric Survey of the Galactic Anti-center (XSTPS-GAC). About 81% of our sample fall into the Stage II phase which is characterized by having optically thick disks, while 14% into the Stage I phase characterized by having significant infalling envelopes, and the remaining 5% into the Stage III phase characterized by having optically thin disks. The median stellar age and mass of the Perseus YSOs are 3.1 Myr and 0.3 $M_\odot$ respectively. By exploring the relationships among the turnoff wave bands $\lambda_{\rm turnoff}$ (longward of which significant IR excesses above the stellar photosphere are observed), the excess spectral index $\alpha_{\rm excess}$ as determined for $\lambda > \lambda_{\rm turnoff}$, and the disk inner radius $R_{\rm in}$ (determined from SED modeling) for YSOs at different evolutionary stages, we found that the median and standard deviation of $\alpha_{\rm excess}$ for YSOs with optically thick disks tend to increase with

** CAS-CONICYT Fellow

$\lambda_{\rm turnoff}$, especially at $\lambda_{\rm turnoff} \geq$5.8 μm, whereas the median fractional dust luminosities $L_{\rm dust}/L_\star$ tend to decrease with increasing $\lambda_{\rm turnoff}$. This points to an inside-out process of disk clearing for small dust grains. Moreover, a positive correlation between $\alpha_{\rm excess}$ and $R_{\rm in}$ was found at $\alpha_{\rm excess} \gtrsim 0$ and $R_{\rm in} \gtrsim 10 \times$ the dust sublimation radius $R_{\rm sub}$, irrespective of $\lambda_{\rm turnoff}$, $L_{\rm dust}/L_\star$ and disk flaring. This suggests that the outer disk flaring either does not evolve synchronously with the inside-out disk clearing of small dust grains or has little appreciable influence on the spectral slopes at $\lambda \lesssim 24$ μm. About 23% of our YSO disks are classified as transitional disks, which have $\lambda_{\rm turnoff} \geq 5.8$ μm and $L_{\rm dust}/L_\star > 10^{-3}$. The transitional disks and full disks occupy distinctly different regions on the $L_{\rm dust}/L_\star$ vs. $\alpha_{\rm excess}$ diagram. Taking $L_{\rm dust}/L_\star$ as an approximate discriminator of disks with (>0.1) and without (<0.1) considerable accretion activity, we found that 65% and 35% of the transitional disks may be consistent with being dominantly cleared by photoevaporation and dynamical interaction with giant planets respectively. None of our transitional disks have $\alpha_{\rm excess}$ (<0.0) or $L_{\rm dust}/L_\star$ (>0.1) values that would otherwise be suggestive of disk clearing dominanted by grain growth.

Key words: stars: formation — stars: low-mass — stars: pre-main sequence — individual: Perseus Cloud — circumstellar matter — protoplanetary

1 INTRODUCTION

The formation and early evolution of stars are among the central problems in astrophysics. Young stellar objects (YSOs), which are primarily identified as pre-main-sequence (PMS) stars by the presence of infrared (IR) excess arising from circumstellar disks or surrounding envelopes (e.g. Allen et al. 2004; Greene et al. 1994; Lada 1987), have been extensively studied in nearby star-forming regions (e.g. Taurus: Luhman et al. 2010; NGC 1333: Winston et al. 2010; IC 348: Muench et al. 2007; σ Ori: Hernández et al. 2007a; Tr 37: Sicilia-Aguilar et al. 2006; NGC 2362: Currie & Kenyon 2009; Lynds 1630N and Lynds 1641: Fang et al. 2009, 2013). Studying the circumstellar environment, either disks or envelopes, around YSOs with different masses is essential to understanding the formation of both stars and their planetary systems.

YSOs are traditionally categorized into four classes or evolutionary stages based on the spectral index α ($d\log(\lambda F(\lambda))/d\log(\lambda)$) of their near- to mid-IR spectral energy distributions (SEDs; e.g. Andre et al. 1993; Greene et al. 1994; Lada 1987). The youngest Class 0 objects are only visible in far-IR to submm wavelengths, and they are thought to have envelope mass that exceeds the central stellar mass; Class I YSOs ($\alpha \geq 0.3$) are characterized by rising mid-IR SEDs, and may still be in an envelope collapse stage but have central stellar mass exceeding the envelope mass; Class II YSOs ($-1.6 \leq \alpha < -0.3$) have SEDs that peak at near-IR wavelengths, decrease at longer wavelengths which is much more gradual than what is expected for a stellar photosphere, and they agree well with PMS stars with circumstellar accretion disks; Class III YSOs ($\alpha < -1.6$) have little or no IR excess, and are thought to be in the disk dissipation stage with very little or no circumstellar material. In addition, Greene et al. (1994) introduced an additional FLAT-spectrum class ($-0.3 \leq \alpha < 0.3$) which has spectral indices in between Classes I and II.

The star formation process is generally accompanied by the formation, evolution and dispersal of circumstellar protoplanetary disks which are believed to be the sites of planet formation. In particular, optically thick full disks are usually found in the Class II YSOs, whereas the evolved or anemic optically thin disks are usually identified with the Class III YSOs. A lot of important information about the evolutionary stages and disk properties of YSOs is encoded in the multi-wavelength SEDs (e.g. Robitaille et al. 2006, hereafter R06). For instance, the optical to near-IR bands offer important constraints on the properties of the central source, such as the temperature and bolometric luminosity; the near- to mid-IR bands provide a crucial constraint on the inner (from a few AU to tens of AU) disk properties; the far-IR to submm bands give strong constraints on the mass of disks and envelopes (e.g. Andrews & Williams 2005).

As currently the most active site of low- to intermediate-mass star formation within ∼300 pc of the Sun, the region encompassing the Perseus molecular cloud ($M \simeq 4.8\times10^3$ $M_\odot$; Evans et al. 2009) is an ideal laboratory for studying the formation and early evolution of low- to intermediate-mass stars (e.g. Bally et al. 2008) and the circumstellar disks. Recently, observations with the *Spitzer* telescope, especially through the "Cores to Disks" legacy project (c2d; Evans et al. 2003), have led to the identification of over 400 YSOs (mostly Classes I and II) toward the Perseus molecular cloud. In addition, systematic submm continuum surveys of the Perseus region with SCUBA (Hatchell et al. 2005) and Bolocam/CSO (Enoch et al. 2006) have led to the confirmation of over 100 protostellar or starless submm cores, and about one-third (one-fifth) of these cores were classified as Class 0 (Class I) YSOs. About two-thirds of the Perseus YSOs are associated with the two major young clusters NGC 1333 and IC 348, and the remaining YSOs are either associated with other much smaller clouds, such as Barnard 5, Barnard 1, L1455 and L1448, or sparsely distributed across the whole Perseus cloud region (e.g. Evans et al. 2009; Jørgensen et al. 2007).

A systematic investigation of the evolutionary stages and disk properties of the Perseus YSOs with optical-to-IR SEDs is still lacking. Moderately deep broadband gri imaging data were recently obtained through Purple Mountain Observatory's (PMO's) Xuyi Schmidt Telescope Photometric Survey of the Galactic Anti-center (XSTPS-GAC; Liu et al. 2014; Zhang et al. 2013, 2014; Yuan et al. 2015, in preparation). In this paper, we combine the gri data with the IR data from 2MASS, *Spitzer* and WISE in order to study the physical properties of the central stellar sources, the evolutionary stages and inner disk properties of the Perseus YSOs. Future spectroscopic data from LAMOST (Liu et al. 2015) on most of those YSOs will provide further details on the disk accretion properties, and thus enhance the broad-band characterization offered in this paper. Section 2 introduces the data and YSO sample analyzed in this work. The color-magnitude diagrams are presented in Section 3. Section 4 presents the results from SED modeling, such as the central stellar masses, ages and the evolutionary stages of the YSOs. An investigation of the excess dust emission and disk geometry parameters, such as the disk inner radii and outer disk flaring, and implications on the dominant disk clearing processes, are given in Section 5. A brief summary of the main results in this work is given in Section 6.

2 SAMPLE AND DATA

2.1 Parent Sample of Perseus YSOs

The most recent census of Perseus YSOs was done by Hsieh & Lai (2013) (HL13), using photometric data from the *Spitzer* c2d legacy project (Evans et al. 2009), which carried out a wide-field imaging survey of five nearby low-mass star-forming clouds (Serpens, Perseus, Ophiuchus, Lupus and Chamaeleon) with both IRAC and MIPS instruments onboard *Spitzer*, instead of simply relying on a cut on a one or two color-color diagram and a color-magnitude diagram to separate YSOs in a multi-dimensional magnitude space.

In particular, HL13 used data from the *Spitzer* SWIRE survey of the ELAIS N1 extragalactic field (Surace et al. 2004) to acquire a control sample for background galaxies, and this control sample was used to define the regions occupied by galaxies in the multi-dimensional magnitude space. The readers are referred to HL13 for more details about the YSO identification procedure. In total, HL13 identified 469 Perseus YSOs over 3.86 deg^2 covered by the c2d survey. Adopting a distance of 250 pc for the Perseus cloud, 3.86 deg^2 corresponds to about 73.6 pc^2 (Evans et al. 2009). Among the 469 YSOs, 21% were classified as Class 0/I sources, 10% as Class FLAT sources, 58% as Class II sources, and 10% as Class III sources based on the 2MASS K_s to MIPS 24 μm spectral indices

α. We note that 429 of the 469 YSOs have detections in at least three IR bands, and thus the identification of these 429 YSOs in the multi-magnitude space should be more reliable than the other 40. In the following, the 429 YSOs will be regarded as the parent sample, and our subsample selection and analysis will be based on these 429 YSOs.

2.2 Data

2.2.1 Broadband gri photometry from XSTPS-GAC

From the fall of 2009 to the spring of 2011, the XSTPS-GAC observing project carried out an imaging survey toward the Galactic Anti-center in SDSS gri bands with the PMO's Xuyi 1.04/1.20m Schmidt Telescope. This survey covers the sky area from RA $\sim 45^\circ$ to 135° and DEC $\sim -10^\circ$ to 60°, plus an extension of ~ 900 deg^2 toward the direction of M31/M33. With an exposure time of 90 seconds, the survey reaches $r_{\rm lim} \sim 19$ in the r band at 10σ for point sources. The astrometry (accurate to $\sim 0.1''$) was calibrated against the PPMXL catalog (Roeser et al. 2010), and the PSF-fitting photometry was calibrated against the SDSS DR8 catalog using the overlapping sky area with an accuracy of 2%. Given the importance of optical bands in constraining the properties of central stellar sources of YSOs, XSTPS-GAC point sources with signal-to-noise ratio (S/N) >2 ($r_{\rm lim} \simeq 21$ mag) will be used in this work.

2.2.2 Spitzer data from the c2d project

As mentioned above, the Perseus cloud has been observed by the c2d project in the *Spitzer* IRAC 3.6 (IR1), 4.5 (IR2), 5.8 (IR3) and 7.9 (IR4) μm and MIPS 24 (M1), 70 (M2) and 160 (M3) μm bands. All data, including imagery and point-source photometry (through PSF fitting) catalogs for IRAC, M1 and M2 were processed and released by the c2d team. In this work, we used the high reliability (HREL) source catalog provided by the c2d project[1].

2.2.3 2MASS and WISE data

The JHK_s photometry was taken from the 2MASS Point Source Catalog which reaches a K_s-band limiting magnitude of 14.3 mag at 10σ. The Wide-field Survey Explorer (WISE) survey mapped the whole sky in four IR broadbands, i.e. 3.4 (W1), 4.6 (W2), 12 (W3) and 22 (W4) μm, with a 5σ limiting magnitude of 16.6, 15.6, 11.3 and 8.0 mag respectively for the four bands. In this work, we used the ALLWISE Source Catalog[2] which includes enhanced photometric sensitivity and accuracy, and improved astrometric precision compared to the 2012 WISE All-Sky Data Release.

2.3 Our Working Sample

In this work, we selected a subsample of 211 Perseus YSOs from the HL13 parent sample. The 211 YSOs were selected by cross-matching the HL13 catalog with all the above data sets, with a requirement that each source should have JHK_s, IRAC or WISE, M1 or W4, and at least one optical band available. Among the 211 YSOs, 102 have g-band detections with S/N > 2, 151 have r-band detections, and 198 have i-band detections. We point out that 78% (99%) of the g-band detections have S/N > 10 (5), 85% (99%) of the r-band detections have S/N > 10 (5), and 94% (100%) of the i-band detections have S/N > 10 (5). In addition, 27 of our sample YSOs have M2 detections. Optical photometry of the 211 YSOs is given in Table 1.

[1] *http://irsa.ipac.caltech.edu/data/SPITZER/C2D/*
[2] *http://wise2.ipac.caltech.edu/docs/release/allwise/*

Table 1 Optical Photometry of Perseus YSOs

ID_{c2d}	R.A.(J2000) (deg)	Dec.(J2000) (deg)	g (mag)	σ_g (mag)	r (mag)	σ_r (mag)	i (mag)	σ_i (mag)
			J band turnoff[3]					
c2dJ032852.2+304506	52.21736	30.75154	13.96	0.06	12.9	0.06		
c2dJ032854.6+311651	52.22763	31.28086			18.73	0.08	16.7	0.06
c2dJ032917.7+312245	52.32366	31.37917	15.55	0.06	13.82	0.05		
c2dJ033035.5+311559	52.64781	31.26627	18.78	0.07	18.0	0.07	17.05	0.06
c2dJ033330.4+311051	53.37669	31.18071	15.99	0.05	13.98	0.06		
c2dJ034157.4+314837	55.48934	31.81021	18.38	0.06	16.22	0.06	14.7	0.06
c2dJ034344.5+314309	55.93535	31.71926	18.69	0.06	17.19	0.06	14.52	0.06
c2dJ034413.0+320135	56.05407	32.02652					18.99	0.13
c2dJ034441.2+321010	56.17156	32.16944					17.4	0.07
			H band turnoff					
c2dJ032519.5+303424	51.33134	30.57338	19.24	0.07	18.75	0.09	18.34	0.06
c2dJ033037.0+303128	52.65402	30.52437	20.41	0.11	17.82	0.06	15.82	0.06
c2dJ033044.0+303247	52.68326	30.54639	16.13	0.07	14.55	0.07	13.21	0.08
c2dJ033118.3+304940	52.82625	30.82765	18.11	0.06	15.31	0.06	14.48	0.06
c2dJ033312.8+312124	53.30349	31.35673			19.61	0.13	17.88	0.06
c2dJ033341.3+311341	53.42204	31.22806	20.9	0.32	18.52	0.07	17.73	0.06
c2dJ034109.1+314438	55.28804	31.74386	17.63	0.06	15.18	0.06	14.28	0.06
c2dJ034255.9+315842	55.73312	31.97834	14.69	0.06	13.45	0.06		
c2dJ034426.7+320820	56.11124	32.13898	19.45	0.12	18.34	0.08	16.7	0.06
c2dJ034431.1+321848	56.12973	32.31347			19.86	0.37	18.09	0.08
c2dJ034437.9+320804	56.15785	32.13448	18.1	0.06	16.13	0.06	14.87	0.06
c2dJ034516.3+320620	56.31809	32.10559	18.33	0.06	16.19	0.06	14.85	0.06
c2dJ034520.5+320634	56.33525	32.10958	17.57	0.06	15.39	0.06	14.1	0.06
			K_s band turnoff					
c2dJ032741.5+302017	51.92281	30.33799	16.46	0.06	14.74	0.06		
c2dJ032800.1+300847	52.00038	30.1464	19.82	0.08	17.32	0.06	15.13	0.07
c2dJ032847.6+312406	52.19853	31.40168					19.64	0.11
c2dJ032850.6+304245	52.2109	30.7124					20.31	0.28
c2dJ032851.0+311818	52.21262	31.30513	18.49	0.07	15.81	0.07	14.0	0.07
c2dJ032851.2+311955	52.21335	31.3319	18.19	0.06	15.94	0.06	14.7	0.06
c2dJ032859.6+312147	52.24817	31.36296	18.42	0.06	16.13	0.06	15.59	0.06
c2dJ032903.8+311604	52.26574	31.26773	20.12	0.13	17.61	0.07	16.01	0.06
c2dJ032903.9+305630	52.26613	30.9416					18.87	0.07
c2dJ032903.9+312149	52.26614	31.3635	17.15	0.07	15.28	0.08	14.18	0.07
c2dJ032909.0+312624	52.28738	31.43997					19.95	0.17
c2dJ032910.8+311643	52.29515	31.27849			19.79	0.16	18.71	0.07
c2dJ032913.1+312253	52.30474	31.38134			19.71	0.19	17.3	0.07
c2dJ032921.9+311536	52.34115	31.26005	15.29	0.05	14.96	0.06	13.49	0.06
c2dJ032923.2+312030	52.34653	31.34173	18.59	0.06	16.9	0.06	15.14	0.06
c2dJ032932.6+312437	52.38573	31.41025			17.79	0.06	16.65	0.06
c2dJ033001.9+303529	52.5078	30.59145			19.09	0.1	18.21	0.08
c2dJ033035.9+303024	52.64968	30.50678			12.07	0.07		
c2dJ033038.2+303212	52.65919	30.53665			19.7	0.2	18.44	0.07
c2dJ033052.5+305418	52.71878	30.90494			19.05	0.12	17.14	0.06
c2dJ033114.7+304955	52.81127	30.83206	18.53	0.06	16.91	0.06	15.8	0.06
c2dJ033142.4+310625	52.92668	31.10691	19.8	0.1	17.66	0.06	15.8	0.06
c2dJ033233.0+310222	53.13745	31.03935	20.13	0.11	17.84	0.06	15.38	0.06
c2dJ033234.0+310056	53.14185	31.01549	18.02	0.06	15.79	0.06	14.34	0.06
c2dJ033241.7+311046	53.17377	31.17953	20.63	0.2	18.35	0.07	16.65	0.06

[3] The YSOs start exhibiting significant (3σ) IR excesses above the photosphere level longward of the turnoff wavebands.

Table 1 — *Continued.*

ID_{c2d}	R.A.(J2000) (deg)	Decl.(J2000) (deg)	g (mag)	σ_g (mag)	r (mag)	σ_r (mag)	i (mag)	σ_i (mag)
c2dJ033401.7+311440	53.50692	31.24438	17.86	0.06	15.65	0.06	13.95	0.06
c2dJ033915.8+312431	54.81587	31.40854					18.77	0.07
c2dJ034119.2+320204	55.32994	32.03438	20.07	0.13	17.76	0.07	16.15	0.06
c2dJ034155.7+314811	55.48214	31.80318					20.11	0.12
c2dJ034157.8+314801	55.49064	31.80023			19.16	0.08	16.9	0.06
c2dJ034219.3+314327	55.5803	31.72415			19.56	0.1	17.44	0.06
c2dJ034232.9+314221	55.63711	31.70572			17.63	0.06	16.16	0.06
c2dJ034322.2+314614	55.84257	31.77045			19.32	0.11	17.45	0.06
c2dJ034328.2+320159	55.86753	32.0331	16.88	0.06	15.68	0.06	14.52	0.06
c2dJ034355.2+315532	55.98018	31.92559					18.9	0.08
c2dJ034356.0+320213	55.98346	32.03702	20.51	0.17	18.09	0.07	16.35	0.06
c2dJ034358.6+321728	55.99406	32.29097			16.32	0.1	14.93	0.07
c2dJ034358.9+321127	55.99549	32.19088	18.06	0.06	16.36	0.06	15.3	0.05
c2dJ034359.9+320441	55.9995	32.07817					17.67	0.06
c2dJ034406.0+321532	56.02504	32.25892					17.74	0.07
c2dJ034406.8+320754	56.02833	32.13167	19.46	0.1	17.81	0.07	16.1	0.06
c2dJ034407.5+320409	56.03132	32.0691	20.37	0.17	18.28	0.08	16.48	0.06
c2dJ034411.6+320313	56.04844	32.05364			19.03	0.17	17.22	0.06
c2dJ034418.6+321253	56.07747	32.21475			18.66	0.1	19.08	0.13
c2dJ034421.6+321038	56.0901	32.17713	18.99	0.08	16.85	0.06	15.72	0.06
c2dJ034422.3+321201	56.09307	32.20019	18.31	0.06	16.67	0.06	15.26	0.06
c2dJ034425.5+321131	56.10633	32.192	19.28	0.08	17.22	0.06	15.63	0.06
c2dJ034427.3+321421	56.11359	32.23915	19.42	0.08			16.0	0.06
c2dJ034431.4+320014	56.13069	32.00394					18.56	0.08
c2dJ034435.7+320304	56.1487	32.05097	20.47	0.2	18.88	0.13	17.55	0.06
c2dJ034438.5+320736	56.16024	32.12659	16.84	0.06	15.25	0.06	14.38	0.06
c2dJ034438.5+320801	56.1606	32.13351	18.92	0.07	16.9	0.06	15.21	0.06
c2dJ034444.7+320402	56.18633	32.06736	17.54	0.06	15.42	0.06	14.06	0.06
c2dJ034452.0+322625	56.21668	32.4404			18.83	0.1	16.92	0.06
c2dJ034452.1+315825	56.21689	31.97367					17.71	0.06
c2dJ034525.1+320930	56.35479	32.15842	19.0	0.07	16.85	0.06	15.06	0.06
c2dJ034536.8+322557	56.40347	32.43251	15.96	0.06	13.79	0.05		
c2dJ034548.3+322412	56.45111	32.40334					10.71	0.07
c2dJ034558.2+322647	56.49269	32.44653	20.7	0.29	18.72	0.1	16.73	0.06
IR1 band turnoff								
c2dJ032747.7+301205	51.94864	30.20126			18.17	0.07	16.14	0.07
c2dJ032834.5+310051	52.1437	31.01419					18.38	0.11
c2dJ032842.4+302953	52.17673	30.4981	17.97	0.06	16.28	0.06	14.53	0.06
c2dJ032844.1+312053	52.18372	31.34799					18.34	0.06
c2dJ032846.2+311638	52.19252	31.27734	16.63	0.06	14.93	0.06	13.48	0.06
c2dJ032847.8+311655	52.19933	31.28196	20.02	0.12	19.03	0.08	16.6	0.06
c2dJ032852.2+312245	52.2174	31.37924	17.9	0.06	15.99	0.06	14.64	0.06
c2dJ032856.6+311836	52.23602	31.30987			17.65	0.07	16.28	0.06
c2dJ032857.0+311622	52.23736	31.27285					18.12	0.07
c2dJ032903.1+312238	52.26311	31.37723	20.11	0.14	18.47	0.07	17.06	0.06
c2dJ032904.1+305613	52.26716	30.9369	20.58	0.16	19.41	0.12	17.06	0.06
c2dJ032918.7+312325	52.32808	31.39038	16.0	0.05	14.15	0.06	13.57	0.06
c2dJ032920.4+311834	52.33515	31.3095					18.72	0.13
c2dJ032930.4+311903	52.37668	31.31759	17.57	0.06	16.05	0.06	14.69	0.06
c2dJ032932.9+312713	52.387	31.45349	19.35	0.07	17.67	0.06	15.93	0.06
c2dJ032937.7+312202	52.40723	31.36735			19.71	0.12	17.3	0.06
c2dJ032954.0+312053	52.47518	31.34803	17.81	0.06	15.8	0.06	14.72	0.06

Table 1 — *Continued.*

ID_{c2d}	R.A.(J2000) (deg)	Decl.(J2000) (deg)	g (mag)	σ_g (mag)	r (mag)	σ_r (mag)	i (mag)	σ_i (mag)
c2dJ033024.1+311404	52.60034	31.23454	19.3	0.07	18.0	0.06	16.18	0.06
c2dJ033110.7+304941	52.79451	30.82795	18.55	0.06	15.52	0.06	15.05	0.06
c2dJ033430.8+311324	53.62826	31.22343			18.45	0.07	16.38	0.06
c2dJ033449.8+311550	53.70768	31.26396	15.85	0.06	14.11	0.06		
c2dJ034001.5+311017	55.00621	31.17147			19.56	0.15	17.65	0.06
c2dJ034201.0+314913	55.50422	31.82038					19.16	0.07
c2dJ034204.3+314712	55.51807	31.78655					18.05	0.06
c2dJ034220.3+320531	55.58467	32.09195	20.03	0.12	17.57	0.06	16.14	0.06
c2dJ034232.1+315250	55.63377	31.88043					19.92	0.14
c2dJ034249.2+315011	55.70492	31.83643			19.47	0.1	17.11	0.06
c2dJ034313.7+320045	55.80708	32.01254					18.71	0.08
c2dJ034323.6+321226	55.84821	32.20718			19.32	0.12	17.23	0.06
c2dJ034329.4+315219	55.87265	31.87207					19.38	0.1
c2dJ034345.2+320359	55.9382	32.06628					18.51	0.1
c2dJ034348.8+321552	55.95345	32.26431	19.57	0.13	17.63	0.07	15.95	0.06
c2dJ034355.3+320753	55.98033	32.13147			19.01	0.13	17.04	0.06
c2dJ034359.1+321421	55.99624	32.23923	20.15	0.13	17.61	0.07	16.73	0.06
c2dJ034401.6+322359	56.00656	32.39968			18.68	0.11	16.73	0.06
c2dJ034402.9+315228	56.01215	31.87437					18.9	0.09
c2dJ034418.2+320457	56.0757	32.08249			18.09	0.07	16.4	0.06
c2dJ034425.5+320617	56.10645	32.10476			18.47	0.09	16.77	0.06
c2dJ034426.0+320430	56.10848	32.07512	16.19	0.06	14.19	0.06	13.33	0.06
c2dJ034427.9+322719	56.11625	32.45525	19.42	0.08	17.99	0.07	16.06	0.06
c2dJ034428.5+315954	56.1188	31.99833	18.65	0.06	16.69	0.06	15.03	0.06
c2dJ034429.8+320055	56.12418	32.01516					17.49	0.06
c2dJ034432.0+321144	56.1335	32.19548	15.47	0.06	13.8	0.06	12.77	0.06
c2dJ034433.8+315830	56.1408	31.97506			18.75	0.12	16.88	0.06
c2dJ034435.0+321531	56.1458	32.25865			18.36	0.08	16.5	0.06
c2dJ034435.5+320856	56.14779	32.14897					16.9	0.06
c2dJ034437.0+320645	56.15399	32.11256			12.16	0.06		
c2dJ034437.4+320901	56.1559	32.15024			16.75	0.09	15.54	0.06
c2dJ034438.0+320330	56.15825	32.05825	17.72	0.06	15.43	0.06	14.14	0.06
c2dJ034439.8+321804	56.16583	32.30112	19.6	0.09	17.12	0.06	15.44	0.06
c2dJ034440.2+320933	56.16771	32.15917					17.01	0.08
c2dJ034442.6+321002	56.17741	32.16735					17.97	0.07
c2dJ034443.1+313734	56.17942	31.62603					19.06	0.08
c2dJ034443.8+321030	56.18241	32.1751	20.86	0.24	18.55	0.1	15.89	0.06
c2dJ034450.4+315236	56.20979	31.87667					18.27	0.09
c2dJ034456.1+320915	56.23394	32.15422	17.08	0.06	14.75	0.06	13.77	0.05
c2dJ034517.8+321206	56.32426	32.20162			18.78	0.09	16.78	0.06
c2dJ034529.7+315920	56.37382	31.98881					18.53	0.08
c2dJ034533.5+314555	56.38945	31.76536					19.73	0.13
c2dJ034535.6+315954	56.39849	31.99845					17.88	0.07
c2dJ034657.4+324917	56.7391	32.8215			18.7	0.09	16.86	0.06
IR2 band turnoff								
c2dJ032851.1+311632	52.21281	31.27566	19.99	0.08	18.22	0.07	16.27	0.06
c2dJ032852.2+311547	52.2173	31.26307			19.19	0.1	16.83	0.06
c2dJ032852.9+311626	52.22052	31.274	20.38	0.15	18.47	0.07	16.53	0.06
c2dJ032909.5+312721	52.28954	31.45581			20.12	0.23	17.96	0.06
c2dJ032917.8+311948	52.32406	31.33001					19.35	0.08
c2dJ032921.6+312110	52.33988	31.35287	18.91	0.07	16.85	0.06	15.24	0.06
c2dJ032923.2+312653	52.34687	31.44808	20.04	0.11	18.57	0.07	16.69	0.06

Table 1 — *Continued.*

ID_{c2d}	R.A.(J2000) (deg)	Decl.(J2000) (deg)	g (mag)	σ_g (mag)	r (mag)	σ_r (mag)	i (mag)	σ_i (mag)
c2dJ032928.9+305842	52.37034	30.9783	18.75	0.06	17.2	0.06	15.42	0.06
c2dJ032929.8+312103	52.37415	31.35072	19.65	0.1	17.72	0.06	15.83	0.06
c2dJ032937.6+310249	52.40678	31.04699					17.85	0.06
c2dJ033120.1+304918	52.83379	30.82157			19.16	0.09	17.07	0.06
c2dJ033346.9+305350	53.44552	30.89726	20.43	0.17	18.4	0.07	16.55	0.06
c2dJ034336.0+315009	55.90007	31.83583					19.66	0.09
c2dJ034346.5+321106	55.94357	32.18498					18.76	0.09
c2dJ034347.6+320903	55.94853	32.1507					18.54	0.09
c2dJ034415.8+315937	56.06598	31.99354					17.52	0.06
c2dJ034421.3+321156	56.08878	32.19897	19.09	0.07	16.94	0.06	15.49	0.06
c2dJ034427.2+322029	56.11342	32.34133					17.01	0.06
c2dJ034430.8+320956	56.12848	32.16547	11.93	0.08			11.02	0.15
c2dJ034658.5+324659	56.74379	32.78303			19.22	0.13	17.05	0.06
IR3 band turnoff								
c2dJ032858.1+311804	52.24213	31.30102	19.06	0.07	16.92	0.06	15.65	0.06
c2dJ032908.0+312251	52.28315	31.38095			19.26	0.11	17.22	0.08
c2dJ032912.9+312329	52.30381	31.39147			18.36	0.09	16.65	0.06
c2dJ032916.8+312325	52.32013	31.39031					18.22	0.06
c2dJ032926.8+312648	52.36172	31.44654	15.81	0.05	14.11	0.06		
c2dJ032929.3+311835	52.37198	31.30963	19.27	0.07	17.01	0.06	15.6	0.06
c2dJ034233.1+315215	55.63803	31.87075					18.86	0.08
c2dJ034234.2+315101	55.64244	31.85028					18.23	0.07
c2dJ034250.9+314045	55.71208	31.67921					18.44	0.06
c2dJ034301.9+314436	55.75807	31.74322					19.4	0.08
c2dJ034308.7+315139	55.78628	31.86072					19.06	0.08
c2dJ034344.6+320818	55.93594	32.13827	17.3	0.06	15.46	0.06	14.46	0.05
c2dJ034410.1+320405	56.0422	32.06792			19.2	0.16	16.93	0.06
c2dJ034415.2+321942	56.06348	32.32838					17.6	0.08
c2dJ034418.2+320959	56.07588	32.16648			19.23	0.16	17.14	0.06
c2dJ034422.3+320543	56.09287	32.09521	18.94	0.07	16.87	0.06	15.61	0.06
c2dJ034422.6+320154	56.09409	32.03157	18.87	0.07	16.75	0.06	15.05	0.06
c2dJ034425.7+321549	56.10713	32.26367					18.83	0.14
c2dJ034429.2+320116	56.1218	32.02103					18.9	0.1
c2dJ034429.7+321040	56.12391	32.17772	17.39	0.11	15.87	0.07	14.83	0.06
c2dJ034434.1+321636	56.14225	32.2766					17.57	0.06
c2dJ034434.8+315655	56.14503	31.94866	19.52	0.09	17.47	0.07	15.83	0.06
c2dJ034437.4+321224	56.15584	32.20671			18.47	0.09	16.92	0.06
c2dJ034438.0+321137	56.15838	32.19361			18.3	0.08	16.45	0.06
c2dJ034439.0+320320	56.16238	32.05547			19.05	0.18	17.39	0.06
c2dJ034439.2+322009	56.16331	32.3358	19.89	0.11	17.87	0.06	15.83	0.06
c2dJ034441.7+321202	56.17392	32.20062					16.98	0.06
c2dJ034442.6+320619	56.17758	32.10541	17.01	0.06	15.4	0.06	14.58	0.06
c2dJ034443.0+321560	56.17929	32.26656					18.15	0.07
c2dJ034444.6+320813	56.18579	32.13681	19.53	0.13	17.8	0.06	16.16	0.06
c2dJ034457.9+320402	56.24106	32.0671			18.63	0.1	16.56	0.06
c2dJ034460.0+322233	56.24997	32.37576					17.76	0.06
c2dJ034501.4+320502	56.25595	32.08382	13.76	0.06	12.79	0.05		
c2dJ034504.7+321501	56.2694	32.2503			19.27	0.15	17.14	0.06
c2dJ034513.5+322435	56.30627	32.40966					17.89	0.06
IR4 band turnoff								
c2dJ032854.1+311654	52.22537	31.28172			18.89	0.08	16.59	0.06
c2dJ033027.1+302830	52.61309	30.47493					18.39	0.1

Table 1 — *Continued.*

$\mathrm{ID_{c2d}}$	R.A.(J2000) (deg)	Decl.(J2000) (deg)	g (mag)	σ_g (mag)	r (mag)	σ_r (mag)	i (mag)	σ_i (mag)
c2dJ034227.1+314433	55.613	31.74247			19.17	0.11	17.33	0.06
c2dJ034254.7+314345	55.72778	31.72924	16.22	0.05	14.51	0.06	13.59	0.06
c2dJ034306.8+314821	55.77822	31.80569	20.05	0.12	17.63	0.06	15.63	0.06
c2dJ034419.1+320931	56.07973	32.15869					11.3	0.08
c2dJ034421.6+321510	56.08987	32.25271	18.57	0.1	17.62	0.07	15.83	0.06
c2dJ034431.5+320845	56.13145	32.14581	14.71	0.06	13.4	0.06	12.76	0.06
c2dJ034456.8+315411	56.23684	31.90317					17.45	0.06
c2dJ034507.6+321028	56.28182	32.17441			12.11	0.05		
W3 band turnoff								
c2dJ032916.7+311618	52.31955	31.27171	17.17	0.06	15.52	0.06	13.97	0.06
c2dJ033026.0+310218	52.60821	31.03831	15.27	0.05	13.72	0.05		
c2dJ033351.1+311228	53.46281	31.20772	19.35	0.07	17.03	0.06	14.77	0.06
c2dJ034011.8+315523	55.04929	31.92315	19.42	0.07	17.39	0.06	16.17	0.06

Notes: All the photometry was calibrated against the SDSS DR8 catalog.

Spatial distribution of the Perseus YSOs is shown in Figure 1 and the 110 GHz ^{13}CO integrated intensity map from the Coordinated Molecular Probe Line Extinction Thermal Emission Survey of Star Forming Regions (COMPLETE, Goodman et al. 2005; Ridge et al. 2006) project is overlaid for comparison. As already known, most Perseus YSOs are associated with the two major clusters IC 348 and NGC 1333. In particular, 83 of the 211 YSOs are within 15$'$ ($\sim$1.7 pc at a distance of 320 pc, e.g. Belikov et al. 2002; Evans et al. 2009; Strom et al. 1974; de Zeeuw et al. 1999) of IC 348, and 43 are within 15$'$ ($\sim$1.3 pc at a distance of 250 pc, e.g. Evans et al. 2009) of NGC 1333.

Figure 2 shows histograms of the IR1 mag and the spectral indices $\alpha(K_s{-}\mathrm{M1})$ for the parent sample and our working subsample. As can be seen, our 211 YSOs are expected to be statistically unbiased, at least at IR1 $\lesssim$ 10 mag, which would correspond to a stellar mass of $\sim$ 0.9 $M_\odot$ at an age of $\sim$3 Myr for a distance modulus $(m-M)_0 = 7.5$ (corresponding to a distance of 320 pc for IC 348), according to the PMS evolutionary tracks of Baraffe et al. (1998). Moreover, since hot dust of the circumstellar disks may contribute significantly to the IR1 emission, our subsample of YSOs may be statistically unbiased down to $M_\star$ slightly below 0.9 $M_\odot$. In addition, most of our YSOs have $\alpha \lesssim 0.0$, implying that our subsample is dominated by Classes FLAT, II and III YSOs. The spectral index $\alpha(K_s{-}\mathrm{M1})$ (Evans et al. 2009), which quantifies the spectral slope from K_s to *Spitzer* 24 µm, was obtained from a linear fit to logarithms of all available photometry between K_s and M1. Note that for sources without M1 data, we used the W4 data for determining the spectral indices.

3 COLOR-MAGNITUDE DIAGRAMS

The color-magnitude diagrams for our sample are shown in Figure 3. The evolutionary models for low-mass stars and brown dwarfs from Baraffe et al. (1998) are also plotted in Figure 3 to be compared with our data. When plotting the evolutionary models in Figure 3, the JHK photometry in the CIT system as provided by Baraffe et al. (1998) was transformed to the 2MASS photometric system, and our SDSS i magnitude was transformed to the Cousins I magnitude using the transformation equation determined by Lupton (2005). The transformation equation of Lupton (2005) involves Cousins I, SDSS r and SDSS i. Among the 198 YSOs that have i-band detection, 60 do not have r-band detection. To put these 60 YSOs on the $I-J$ vs. J diagram (right panel of Fig. 3), we adopted a median of $I-i=-0.82$, as determined from the YSOs with both r and i detections, to transform SDSS i to Cousins I.

In Figure 3, most of our YSOs are redder than the pure stellar photosphere emission. A recent study by Chen et al. (2015) found a mean visual interstellar extinction of $\lesssim$1 mag toward the Perseus

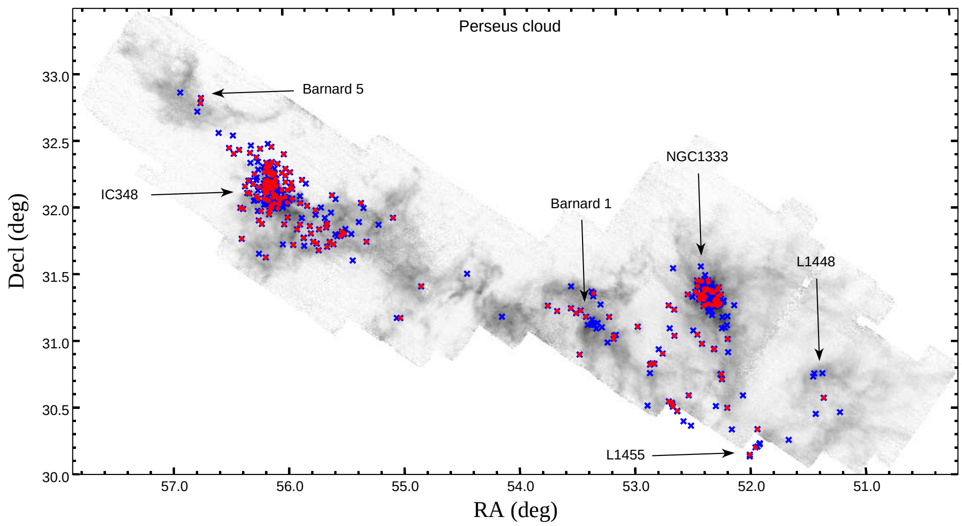

Fig. 1 The spatial distribution of the Perseus YSOs is overplotted on the FCRAO 110 GHz ^{13}CO integrated intensity map (greyscale, FWHM $\simeq 46''$) from the COMPLETE project. The small red circles mark the 211 YSOs studied in this work, and the blue crosses mark the parent sample of 429 YSOs which have at least three band detections in the IR wavelength range from 2MASS J to MIPS 24 µm. Several well-studied clusters or cores are also annotated in the figure.

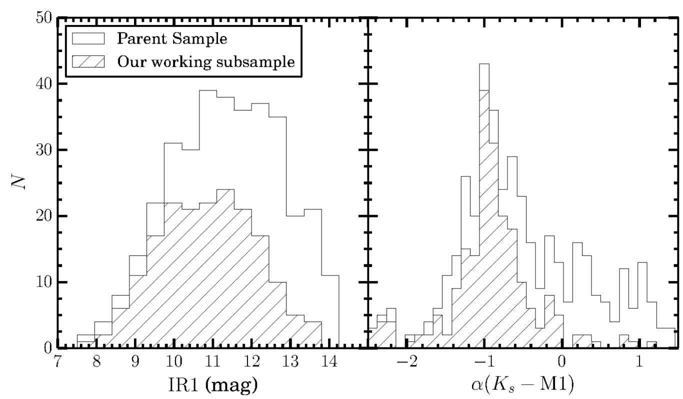

Fig. 2 Histograms of the IRAC 3.6 µm (IR1) magnitude (*left*) and spectral index α (K_s−M1) (*right*) in wavelength ranges from K_s to MIPS 24 µm for the parent sample (*open*) and our working subsample (*hatched*) of YSOs.

region, which is insufficient to explain the red colors of most YSOs, especially considering their distribution on the $J - K_s$ vs. K_s diagram. Therefore, as expected, hot dust emission from the inner circumstellar disks of YSOs contributes significantly to the K_s band. The comparison with theoretical evolutionary tracks implies that the masses of our YSOs are mostly above the substellar limit ($\sim 0.08\ M_\odot$). The fact that evolutionary tracks at different masses and ages are well separated on the color-magnitude diagram involving I band data suggests the importance of optical bands in constraining the properties of the central stellar sources of YSOs.

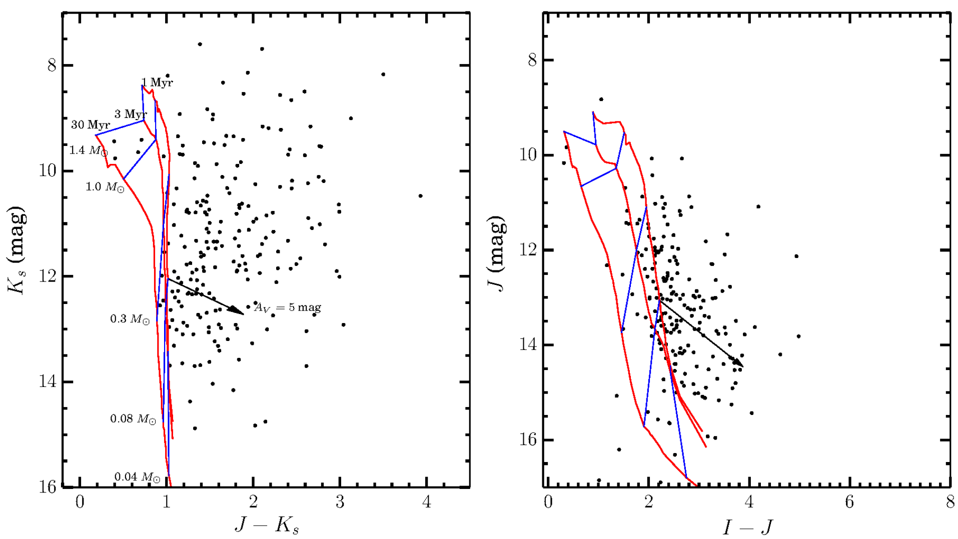

Fig. 3 $J - K_s$ vs. K_s (*left*) and $I - J$ vs. J (*right*) color-magnitude diagrams. The left panel shows the distribution for all of the 211 YSOs (*filled circles*) studied in this work, and the right panel shows the distribution for 198 YSOs with i-band detection. Overplotted are stellar evolutionary tracks of Baraffe et al. (1998) for a stellar mass range of $0.02 - 1.4\ M_\odot$ at three different ages (1, 3 and 30 Myr). The black arrow in each panel marks the 5-mag visual extinction vector, assuming the Fitzpatrick (1999) extinction law with R_V = 3.1. The evolutionary tracks and extinction vector shown in the right panel are the same as those in the left panel. A distance modulus of $(m - M)_0$ = 7.0 for the Perseus YSOs is adopted.

4 SED MODELING

4.1 The Method

With the broadband SEDs in hand, we used the online SED fitting tool developed by R06 and Robitaille et al. (2007) to extract the relevant physical properties of YSOs and their circumstellar disks. This online fitting tool offers the possibility of fitting YSO SEDs with a precomputed grid of 200 000 synthetic SEDs computed at 10 viewing angles. The model SEDs account for the contribution from central stellar photosphere emission, circumstellar disks, and infalling envelopes. In particular, the stellar photosphere emission is modeled with two parameters, i.e. stellar luminosity and temperature; The disk is treated as a standard flaring accretion disk and the resultant emission is modeled with six parameters, i.e. the disk mass ($\sim$0.001–0.1 $M_\odot$), inner radius, outer radius (1–10 000 AU), accretion rate, scale height factor and flaring angle; The envelope emission is modeled with four parameters, i.e. envelope accretion rate, outer radius, cavity density (10^{-22}–8×10^{-20} g cm^{-3}) and cavity opening angle. In addition, the central stellar masses (0.1–50 $M_\odot$) and ages (0.001–10 Myr) are constrained by comparing the stellar luminosity and temperature with the PMS evolutionary tracks of Bernasconi & Maeder (1996) and Siess et al. (2000).

Before proceeding to the SED modeling for our data, we point out some limitations of the R06 SED models (Robitaille 2008) that may be relevant to our current work. Firstly, the models do not include the case for multiple central stellar sources, which can affect the size of the disk/envelope inner holes and thus influence the near- to mid-IR emission. Secondly, there exist several sets of different PMS evolutionary tracks in the literature. Besides the Siess et al. tracks as adopted by the R06 SED models, other popular PMS tracks include Swenson et al. (1994), D'Antona & Mazzitelli (1997), Baraffe et al. (1998), Palla & Stahler (1999), Yi et al. (2003) and Dotter et al. (2008). Adopting different tracks can lead to systematic differences in the fitted stellar parameters (e.g. Fang et al. 2013; Hillenbrand et al. 2008), and the systematic effects are especially significant for sub-solar mass stars at young ages. In particular, uncertainties in age estimation from different tracks for sub-solar mass stars can be up to 0.75 dex at young ages ($<$ 10 Myr, Hillenbrand et al. 2008). Thirdly, the dust opacity law assumed in the models may not be accurate, which would affect the determination of disk/envelope accretion and mass.

When fitting the SEDs, an uncertainty in absolute flux calibration of 5% was added in quadrature to the gri uncertainties, a 10% uncertainty was added to JHK_s and IRAC data uncertainties, and a 20% uncertainty was added to the M2 data uncertainties (Evans et al. 2009). In addition, when both (IR1, IR2) and (W1, W2) data were available, IR1 and IR2 were used in the fitting due to the higher resolution of IRAC data. An aperture of $10''$ was used in the fitting. In addition, the distance to YSOs was allowed to vary from 0.2 to 0.35 kpc, and the foreground interstellar extinction A_V was allowed to vary from 0.3 to 30 mag, with the lower limit of A_V being chosen based on the Perseus extinction map as determined by Chen et al. (2014). Besides the best-fitting model parameters, all the subsequent well-fit models with reduced $\chi^2_{\rm r} - \chi^2_{\rm r,best} < 2$ were used to define the minimum and maximum acceptable physical parameters.

4.2 The Results

The range of wavelength coverage determines what physical parameters can be constrained from SED modeling. A thorough investigation about how the wavelength range of data affects the determination of different physical properties of YSOs was given by R06. Given our wavelength coverage from optical to MIPS 24 μm (or WISE 22 μm), we expect to roughly constrain the central stellar source luminosity, extinction and the circumstellar disk luminosity. Although subject to much larger uncertainties than constraints from spectroscopic data, the central stellar masses and ages can still be roughly constrained from broadband SED modeling to statistically investigate a large sample, like the one presented in this work. Moreover, while the masses of the circumstellar disks and envelopes cannot be reliably constrained unless one has far-IR to submm data, SED modeling for wavelength ranges shorter than far-IR can still be used to statistically constrain the evolutionary stages of YSOs. R06 found that at least three different evolutionary stages of YSOs can be statistically distinguished based on the fitted envelope accretion rates normalized by stellar masses ($\dot{M}_{\rm env}/M_\star$) and disk masses ($M_{\rm disk}/M_\star$). In particular, the Stage I YSOs have significant infalling envelopes and are defined by having $\dot{M}_{\rm env}/M_\star > 10^{-6}$ yr^{-1}; Stage II YSOs have optically thick disks and are defined by having $\dot{M}_{\rm env}/M_\star < 10^{-6}$ yr^{-1} and $M_{\rm disk}/M_\star > 10^{-6}$; Stage III YSOs have optically thin disks and are defined by having both $\dot{M}_{\rm env}/M_\star < 10^{-6}$ yr^{-1} and $M_{\rm disk}/M_\star < 10^{-6}$. Lastly, the near- to mid-IR SEDs are also sensitive to disk properties, such as the disk inner radius and disk flaring.

Figure 4 shows the SEDs of the 27 YSOs which have M2-band detections and at the same time at least one optical band available. The black solid curve in each panel of Figure 4 is the best-fit model SED, and the grey solid curves represent all subsequent well-fit models with reduced $\chi^2_{\rm r} - \chi^2_{\rm r,best} < 2$. In addition, SEDs of the best-fit stellar photosphere emission (corrected for both the interstellar and circumstellar extinction) are overplotted as dashed curves. By calculating the likelihood estimator $e^{-\chi^2_{\rm r}/2}$ for each well-fit model with $\chi^2_{\rm r} - \chi^2_{\rm r,best} < 2$ for a given YSO, we construct the probability density function (PDF) and the corresponding cumulative distribution function (CDF) for parameters such as stellar masses $M_\star$, ages and disk inner radius $R_{\rm in}$. The most probable value for each parameter refers to the median of the corresponding PDF, and the confidence interval is defined as covering the central 95% of the CDF. In what follows in this section, we will present the results for $M_\star$, ages and the evolutionary stages as identified based on the disk masses and envelope accretion rates which are normalized by stellar masses. Discussion about the disk geometry parameters from SED modeling and fractional dust luminosity $L_{\rm dust}/L_\star$, where $L_{\rm dust}$ (in units of $L_\odot$) is equal to the integral of the best-fit stellar photosphere subtracted SEDs, will be presented in the next section. SED modeling results for some relevant parameters, such as $M_\star$, ages and $R_{\rm in}$, are listed in Table 2.

Table 2 SED Fitting Results for Perseus YSOs

$\rm ID_{c2d}$	$\rm ID_{model}$	χ^2_r	A_V	D	$M_\star$	Age$_\star$	$L_\star$	$L_{\rm dust}$	$R_{\rm in}/R_{\rm sub}$	Stage	$\alpha_{\rm turnoff}$	$\alpha_{\rm excess}$
			(mag)	(kpc)	($M_\odot$)	(10^5 yr)	($10^{-2}L_\odot$)	($10^{-2}L_\odot$)				
(1)	(2)	(3)	(4)	(5)	(6)	(7)	(8)	(9)	(10)	(11)	(12)	(13)
						J band turnoff[4]						
c2dJ032852.2+304506	3000104	2.0	3.76	0.28	$2.36^{+0.45}_{-0.22}$	$76.39^{+20.74}_{-23.22}$	5439.09	173.77	$1.7^{+0.7}_{-0.7}$	II	–0.75	–0.63
c2dJ032854.6+311651	3013176	0.4	3.04	0.23	$0.14^{+0.23}_{-0.04}$	$25.55^{+27.4}_{-21.9}$	8.72	1.13	$4.2^{+14.7}_{-3.2}$	II	–0.57	–0.54
c2dJ032917.7+312245	3005510	0.5	5.7	0.26	$2.22^{+0.93}_{-1.11}$	$76.42^{+22.48}_{-66.3}$	2637.26	263.42	$1.1^{+0.5}_{-0.1}$	II	–0.95	–0.8
c2dJ033035.5+311559	3018343	6.7	0.79	0.24	$1.02^{+1.83}_{-0.71}$	$8.92^{+31.75}_{-8.84}$	2475.96	1910.17	$83.9^{+237.7}_{-82.9}$	I	–0.46	–0.14
c2dJ033330.4+311051	3003655	0.3	6.6	0.21	$2.24^{+0.51}_{-0.26}$	$62.4^{+36.51}_{-26.81}$	2561.06	339.83	$1.0^{+-0.0}_{-0.0}$	II	–0.8	–0.99
c2dJ034157.4+314837	3015603	1.3	7.69	0.28	$2.08^{+0.13}_{-0.1}$	$93.61^{+5.3}_{-4.8}$	1964.93	210.13	$1.0^{+0.0}_{-0.0}$	II	–0.86	–1.07
c2dJ034344.5+314309	3017083	2.5	3.27	0.28	$3.11^{+0.3}_{-0.15}$	$16.84^{+59.29}_{-3.08}$	6740.19	123.32	$1.5^{+0.7}_{-0.5}$	II	–0.13	–0.1
c2dJ034413.0+320135	3017363	4.0	5.47	0.23	$3.44^{+0.56}_{-0.52}$	$42.96^{+21.51}_{-17.21}$	17530.01	245.48	$1.5^{+1.4}_{-0.5}$	II	0.71	0.61
c2dJ034441.2+321010	3007882	1.2	4.09	0.3	$0.9^{+2.67}_{-0.63}$	$0.43^{+2.08}_{-0.39}$	3965.79	3561.31	$1.3^{+397.9}_{-0.3}$	I	–0.13	0.14
						H band turnoff						
c2dJ032519.5+303424	3005058	5.5	0.74	0.27	$1.72^{+0.06}_{-0.06}$	$40.9^{+13.71}_{-14.26}$	311.13	4.52	$1.0^{+0.0}_{-0.0}$	II	0.04	0.16
c2dJ033037.0+303128	3000055	1.7	8.57	0.26	$1.49^{+0.9}_{-0.75}$	$26.92^{+63.88}_{-13.42}$	3108.59	95.56	$1.1^{+0.1}_{-0.1}$	III	–0.76	–0.92
c2dJ033044.0+303247	3015197	1.4	3.81	0.24	$0.8^{+2.34}_{-0.47}$	$6.16^{+84.64}_{-3.64}$	142.18	145.99	$1.2^{+5.6}_{-0.2}$	II	–0.58	–0.46
c2dJ033118.3+304940	3002814	2.0	5.21	0.25	$1.49^{+1.15}_{-0.74}$	$31.46^{+64.44}_{-24.58}$	202.82	89.27	$1.5^{+3.6}_{-0.5}$	II	–0.63	–0.65
c2dJ033312.8+312124	3011659	3.8	8.95	0.28	$1.38^{+1.42}_{-1.23}$	$31.73^{+40.29}_{-31.54}$	92.66	507.28	$1.0^{+0.0}_{-0.0}$	I	0.28	0.03
c2dJ033341.3+311341	3003019	2.6	2.59	0.23	$1.88^{+1.06}_{-1.33}$	$13.84^{+76.16}_{-8.62}$	888.1	12.61	$1.7^{+5.1}_{-0.7}$	II	–0.36	–0.29
c2dJ034109.1+314438	3010092	3.5	5.51	0.26	$2.15^{+0.36}_{-1.35}$	$49.38^{+47.77}_{-45.73}$	1686.36	177.4	$1.4^{+2.1}_{-0.4}$	II	–0.51	–0.53
c2dJ034255.9+315842	3019328	4.1	5.23	0.28	$2.29^{+0.02}_{-0.1}$	$65.84^{+10.55}_{-2.06}$	2437.85	62.43	$5.3^{+0.8}_{-4.3}$	III	–0.85	–0.65
c2dJ034426.7+320820	3011061	0.6	0.84	0.3	$0.21^{+0.14}_{-0.06}$	$1.62^{+2.62}_{-0.14}$	37.06	17.83	$1.1^{+0.3}_{-0.1}$	I	–0.44	0.22
c2dJ034431.1+321848	3005792	1.2	3.05	0.26	$0.13^{+1.22}_{-0.03}$	$59.9^{+38.47}_{-57.78}$	3.09	2.97	$3.7^{+11.7}_{-2.7}$	II	–0.61	–0.26
c2dJ034437.9+320804	3002764	0.9	3.92	0.26	$0.8^{+1.99}_{-0.53}$	$19.66^{+54.92}_{-15.99}$	93.56	37.84	$1.3^{+3.3}_{-0.3}$	II	–1.12	–0.95
c2dJ034516.3+320620	3011667	2.6	5.22	0.23	$1.08^{+1.25}_{-0.28}$	$71.65^{+19.15}_{-61.14}$	56.7	49.01	$1.4^{+3.6}_{-0.4}$	II	–0.44	–0.58
c2dJ034520.5+320634	3011715	0.4	4.48	0.28	$1.53^{+1.0}_{-1.11}$	$27.32^{+66.1}_{-21.74}$	266.2	26.14	$1.2^{+2.1}_{-0.2}$	II	–0.72	–0.31
						K_s band turnoff						
c2dJ032741.5+302017	3001576	0.2	2.27	0.24	$0.86^{+0.97}_{-0.43}$	$31.32^{+62.1}_{-21.27}$	49.74	8.74	$1.7^{+3.6}_{-0.7}$	II	–0.67	–0.24
c2dJ032800.1+300847	3000691	2.0	2.53	0.22	$0.19^{+0.26}_{-0.08}$	$5.3^{+18.02}_{-3.45}$	25.08	7.42	$1.2^{+1.7}_{-0.2}$	II	–0.64	–0.14
c2dJ032847.6+312406	3000851	0.2	8.46	0.23	$0.18^{+1.05}_{-0.07}$	$12.99^{+63.88}_{-10.93}$	19.85	1.85	$1.3^{+2.6}_{-0.3}$	II	–1.07	–0.58
c2dJ032850.6+304245	3014369	1.5	5.59	0.25	$0.57^{+1.21}_{-0.46}$	$11.45^{+84.08}_{-9.57}$	36.24	5.12	$3.4^{+31.8}_{-2.4}$	II	0.04	0.16
c2dJ032851.0+311818	3017528	3.1	5.9	0.24	$1.73^{+0.37}_{-0.96}$	$45.46^{+50.44}_{-38.29}$	526.49	66.46	$2.0^{+5.3}_{-1.0}$	II	–0.65	–0.34
c2dJ032851.2+311955	3013451	1.5	4.15	0.23	$1.11^{+1.06}_{-0.61}$	$32.15^{+61.02}_{-25.55}$	169.12	18.34	$10.8^{+7.4}_{-9.8}$	III	–0.61	–0.19
c2dJ032859.6+312147	3015522	3.6	2.25	0.2	$2.24^{+0.32}_{-0.88}$	$13.53^{+10.05}_{-3.7}$	904.71	12.41	$1.6^{+1.6}_{-0.6}$	II	–0.77	–0.55
c2dJ032903.8+311604	3005745	2.3	4.9	0.25	$0.82^{+1.21}_{-0.65}$	$0.07^{+0.78}_{-0.06}$	1419.57	2497.43	$3.7^{+5.2}_{-2.7}$	I	0.99	1.13
c2dJ032903.9+305630	3005573	1.7	0.65	0.25	$0.14^{+0.08}_{-0.04}$	$1.19^{+5.31}_{-1.02}$	14.67	5.3	$13.6^{+24.6}_{-12.6}$	I	0.01	0.75
c2dJ032903.9+312149	3001003	1.4	3.29	0.23	$0.99^{+1.91}_{-0.55}$	$7.14^{+69.25}_{-5.74}$	206.45	25.3	$2.0^{+3.4}_{-1.0}$	II	–0.63	–0.23
c2dJ032909.0+312624	3013017	2.0	2.11	0.22	$0.59^{+1.16}_{-0.48}$	$5.67^{+79.27}_{-5.66}$	102.75	0.72	$2.2^{+5.4}_{-1.2}$	II	0.1	0.5
c2dJ032910.8+311643	3005025	2.7	1.25	0.24	$0.3^{+0.21}_{-0.19}$	$6.78^{+3.26}_{-2.22}$	11.28	2.45	$5.2^{+4.3}_{-4.2}$	I	–0.05	0.3
c2dJ032913.1+312253	3012963	0.2	2.57	0.22	$0.27^{+1.51}_{-0.15}$	$0.9^{+3.96}_{-0.61}$	90.31	53.94	$1.2^{+1.7}_{-0.2}$	I	–0.8	–0.3
c2dJ032921.9+311536	3018372	6.0	0.77	0.22	$0.2^{+0.07}_{-0.07}$	$4.09^{+11.73}_{-3.01}$	34.96	14.09	$1.2^{+0.4}_{-0.2}$	II	–1.11	–0.82
c2dJ032923.2+312030	3009928	0.3	0.89	0.24	$0.13^{+0.2}_{-0.03}$	$14.37^{+27.48}_{-11.44}$	7.74	2.33	$1.8^{+8.9}_{-0.8}$	II	–0.69	0.03
c2dJ032932.6+312437	3003831	0.8	1.99	0.23	$0.69^{+1.36}_{-0.53}$	$13.76^{+51.54}_{-7.61}$	139.55	2.06	$1.3^{+1.2}_{-0.3}$	II	–0.91	–0.38
c2dJ033001.9+303529	3010577	4.2	0.78	0.24	$0.39^{+0.13}_{-0.06}$	$8.17^{+0.31}_{-0.14}$	79.42	1.64	$1.8^{+1.7}_{-0.8}$	II	0.82	1.06
c2dJ033035.9+303024	3009292	0.4	3.7	0.22	$2.23^{+0.67}_{-0.44}$	$39.41^{+45.77}_{-29.54}$	1083.2	125.66	$1.4^{+3.5}_{-0.4}$	II	–0.94	–0.87

[4] The YSOs start exhibiting significant (3σ) IR excesses above the photosphere level longward of the turnoff wavebands.

Table 2 — *Continued.*

ID_{c2d}	ID_{model}	χ_r^2	A_V	D	$M_\star$	Age$_\star$	$L_\star$	L_{dust}	R_{in}/R_{sub}	Stage	$\alpha_{turnoff}$	α_{excess}
			(mag)	(kpc)	($M_\odot$)	(10^5 yr)	($10^{-2} L_\odot$)	($10^{-2} L_\odot$)				
(1)	(2)	(3)	(4)	(5)	(6)	(7)	(8)	(9)	(10)	(11)	(12)	(13)
c2dJ033038.2+303212	3002146	1.6	0.9	0.24	$0.35^{+0.13}_{-0.13}$	$0.26^{+1.62}_{-0.16}$	179.08	170.26	$55.6^{+423.3}_{-54.6}$	I	0.67	1.76
c2dJ033052.5+305418	3010241	0.6	6.53	0.23	$0.57^{+1.07}_{-0.46}$	$31.83^{+61.34}_{-27.74}$	44.73	10.54	$1.3^{+13.2}_{-0.3}$	II	–0.24	–0.18
c2dJ033114.7+304955	3002775	2.4	2.89	0.25	$2.41^{+0.5}_{-1.06}$	$8.33^{+3.41}_{-2.65}$	1011.41	23.12	$4.0^{+3.6}_{-2.5}$	II	0.04	0.01
c2dJ033142.4+310625	3016509	0.7	3.17	0.23	$0.31^{+0.28}_{-0.19}$	$19.2^{+37.9}_{-16.06}$	37.18	3.41	$1.3^{+3.0}_{-0.3}$	II	–1.16	–0.63
c2dJ033233.0+310222	3014845	3.6	3.21	0.22	$0.2^{+0.19}_{-0.09}$	$5.76^{+13.31}_{-4.88}$	68.83	16.19	$5.0^{+1.9}_{-4.0}$	II	–0.89	–0.58
c2dJ033234.0+310056	3000422	1.2	4.43	0.25	$1.38^{+1.08}_{-0.94}$	$22.39^{+76.7}_{-14.91}$	193.4	50.34	$1.2^{+2.0}_{-0.2}$	II	–0.46	–0.28
c2dJ033241.7+311046	3010765	0.5	5.88	0.24	$0.57^{+0.18}_{-0.46}$	$64.2^{+30.92}_{-61.8}$	32.03	19.97	$2.0^{+13.6}_{-1.0}$	II	–0.29	–0.01
c2dJ033401.7+311440	3009679	0.8	2.88	0.23	$0.42^{+0.43}_{-0.1}$	$9.33^{+4.96}_{-4.2}$	52.2	8.88	$3.7^{+4.0}_{-2.7}$	II	–0.92	–0.7
c2dJ033915.8+312431	3007253	0.4	6.85	0.24	$0.33^{+1.03}_{-0.22}$	$35.06^{+54.21}_{-32.25}$	11.25	4.04	$1.9^{+6.3}_{-0.9}$	II	–0.71	–0.24
c2dJ034119.2+320204	3002434	0.6	3.78	0.23	$0.47^{+0.92}_{-0.36}$	$43.27^{+47.35}_{-37.0}$	17.44	2.42	$1.5^{+3.4}_{-0.5}$	II	–1.19	–0.89
c2dJ034155.7+314811	3008064	3.0	5.71	0.22	$1.28^{+1.13}_{-0.96}$	$6.5^{+21.64}_{-0.81}$	499.65	12.91	$5.2^{+1.1}_{-1.6}$	II	0.27	–0.03
c2dJ034157.8+314801	3007280	0.4	8.27	0.25	$1.02^{+0.75}_{-0.87}$	$22.39^{+72.52}_{-21.01}$	178.8	19.86	$2.2^{+5.8}_{-1.2}$	II	–0.71	–0.36
c2dJ034219.3+314327	3017857	1.3	7.04	0.24	$0.69^{+1.64}_{-0.3}$	$37.15^{+57.97}_{-30.81}$	416.8	9.03	$1.8^{+4.1}_{-0.8}$	II	–0.4	–0.25
c2dJ034232.9+314221	3016488	0.4	5.11	0.24	$0.78^{+0.93}_{-0.47}$	$51.63^{+44.93}_{-41.79}$	86.93	8.22	$1.8^{+6.0}_{-0.8}$	II	–0.66	–0.17
c2dJ034322.2+314614	3005663	0.7	5.71	0.24	$0.5^{+1.33}_{-0.39}$	$24.68^{+64.75}_{-22.92}$	26.44	4.09	$1.3^{+3.0}_{-0.3}$	II	–0.95	–0.53
c2dJ034328.2+320159	3018372	0.6	1.42	0.26	$0.21^{+0.33}_{-0.07}$	$7.2^{+36.93}_{-5.58}$	34.96	13.02	$1.2^{+1.5}_{-0.2}$	II	–1.21	–0.91
c2dJ034355.2+315532	3002726	0.5	3.03	0.25	$0.19^{+1.29}_{-0.08}$	$2.52^{+21.0}_{-1.52}$	41.19	27.18	$1.2^{+1.4}_{-0.2}$	I	–0.56	0.32
c2dJ034356.0+320213	3005130	0.8	5.05	0.25	$0.71^{+2.09}_{-0.48}$	$4.63^{+86.17}_{-3.46}$	300.35	187.54	$1.7^{+3.2}_{-0.7}$	I	–0.82	–0.49
c2dJ034358.6+321728	3010994	0.2	3.26	0.28	$0.64^{+0.82}_{-0.51}$	$33.03^{+59.16}_{-29.73}$	33.09	6.74	$2.2^{+7.8}_{-1.2}$	II	–0.83	–0.27
c2dJ034358.9+321127	3004698	1.7	2.92	0.28	$0.57^{+1.71}_{-0.43}$	$21.17^{+42.97}_{-19.34}$	599.4	13.65	$2.9^{+4.0}_{-1.9}$	II	–0.43	0.28
c2dJ034359.9+320441	3012322	0.4	2.99	0.29	$0.16^{+0.18}_{-0.06}$	$67.5^{+29.94}_{-50.52}$	4.42	0.98	$9.9^{+24.0}_{-8.9}$	II	–0.95	–0.03
c2dJ034406.0+321532	3013554	0.4	2.51	0.3	$0.14^{+0.15}_{-0.04}$	$75.1^{+22.5}_{-53.34}$	2.21	0.57	$2.7^{+10.8}_{-1.7}$	II	–1.06	–0.5
c2dJ034406.8+320754	3014099	0.2	1.58	0.28	$0.15^{+0.24}_{-0.04}$	$27.98^{+48.22}_{-24.21}$	10.85	3.9	$2.2^{+8.5}_{-1.2}$	II	–0.97	–0.32
c2dJ034407.5+320409	3006323	1.2	1.81	0.29	$0.19^{+0.26}_{-0.08}$	$5.75^{+63.18}_{-5.45}$	87.35	24.56	$89.6^{+33.3}_{-88.6}$	II	0.1	1.3
c2dJ034411.6+320313	3017532	0.5	8.63	0.29	$1.29^{+0.86}_{-0.86}$	$23.94^{+70.98}_{-17.17}$	111.11	28.32	$1.5^{+2.9}_{-0.5}$	II	-0.95	–0.63
c2dJ034418.6+321253	3005247	0.5	7.88	0.24	$0.19^{+1.65}_{-0.08}$	$8.93^{+77.73}_{-8.07}$	19.68	10.88	$1.6^{+4.6}_{-0.6}$	II	–0.84	–0.78
c2dJ034421.6+321038	3015022	0.6	3.27	0.25	$1.34^{+1.55}_{-0.92}$	$9.54^{+65.04}_{-6.48}$	239.74	18.36	$1.3^{+2.0}_{-0.3}$	II	–1.0	–0.72
c2dJ034422.3+321201	3016057	0.4	2.41	0.25	$0.36^{+0.26}_{-0.26}$	$37.51^{+51.77}_{-31.02}$	12.59	2.74	$2.0^{+5.0}_{-1.0}$	II	–1.01	–0.63
c2dJ034425.5+321131	3014369	1.2	4.33	0.26	$0.56^{+1.6}_{-0.41}$	$31.08^{+36.08}_{-27.33}$	36.24	21.18	$2.9^{+7.6}_{-1.9}$	II	–0.53	–0.24
c2dJ034427.3+321421	3010010	0.5	2.5	0.28	$0.3^{+0.67}_{-0.2}$	$36.19^{+53.09}_{-32.14}$	11.86	4.54	$2.6^{+10.4}_{-1.6}$	II	–0.96	–0.28
c2dJ034431.4+320014	3007448	0.3	10.18	0.28	$1.01^{+0.81}_{-0.78}$	$22.73^{+71.69}_{-19.04}$	47.14	12.0	$1.9^{+5.8}_{-0.9}$	II	–0.88	–0.58
c2dJ034435.7+320304	3018693	0.6	2.74	0.26	$0.31^{+1.46}_{-0.21}$	$15.19^{+72.83}_{-11.83}$	194.13	4.48	$1.7^{+6.4}_{-0.7}$	II	–0.27	0.42
c2dJ034438.5+320736	3005663	3.5	2.35	0.23	$0.45^{+0.57}_{-0.29}$	$21.09^{+45.4}_{-19.47}$	26.44	9.05	$1.8^{+5.4}_{-0.8}$	II	–0.82	–0.26
c2dJ034438.5+320801	3000691	0.7	2.01	0.26	$0.21^{+0.24}_{-0.1}$	$11.49^{+16.18}_{-10.47}$	25.08	8.14	$8.0^{+29.6}_{-7.0}$	II	–0.7	0.31
c2dJ034444.7+320402	3014306	0.4	4.54	0.29	$1.73^{+1.18}_{-1.31}$	$21.04^{+72.38}_{-17.14}$	845.66	21.02	$1.3^{+3.9}_{-0.3}$	II	–0.92	–0.33
c2dJ034452.0+322625	3002305	0.6	3.48	0.23	$0.26^{+0.42}_{-0.15}$	$53.98^{+42.12}_{-47.55}$	8.36	0.85	$1.3^{+2.6}_{-0.3}$	II	–1.55	–1.02
c2dJ034452.1+315825	3002882	0.1	4.97	0.28	$0.27^{+0.71}_{-0.17}$	$34.99^{+57.67}_{-31.73}$	35.96	2.84	$1.4^{+4.1}_{-0.4}$	II	–1.05	–0.32
c2dJ034525.1+320930	3011159	1.4	2.34	0.24	$0.23^{+0.31}_{-0.12}$	$11.69^{+19.06}_{-10.86}$	37.64	16.06	$5.1^{+15.1}_{-4.1}$	II	–0.5	0.01
c2dJ034536.8+322557	3017240	0.4	3.33	0.24	$1.49^{+0.51}_{-0.86}$	$22.97^{+53.94}_{-16.05}$	160.5	25.0	$1.3^{+2.1}_{-0.3}$	II	–0.99	–0.29
c2dJ034548.3+322412	3002927	1.9	0.38	0.24	$2.69^{+1.26}_{-1.05}$	$2.24^{+1.33}_{-1.38}$	2822.59	614.5	$1.0^{+0.0}_{-0.0}$	I	–0.72	–0.11
c2dJ034558.2+322647	3000861	0.6	2.34	0.24	$0.17^{+0.18}_{-0.06}$	$53.97^{+39.59}_{-44.72}$	9.78	1.04	$1.5^{+3.1}_{-0.5}$	II	–1.33	–0.8
IR1 band turnoff												
c2dJ032747.7+301205	3015087	1.1	11.48	0.23	$2.65^{+0.73}_{-1.11}$	$33.44^{+33.19}_{-23.92}$	418.98	270.51	$3.2^{+4.6}_{-2.2}$	II	–0.21	–0.52
c2dJ032834.5+310051	3000103	4.1	5.73	0.25	$2.08^{+1.66}_{-1.95}$	$3.88^{+4.02}_{-3.84}$	2102.0	79.64	$5.7^{+3.8}_{-4.7}$	II	0.75	0.24
c2dJ032842.4+302953	3010255	0.3	0.85	0.23	$0.16^{+0.11}_{-0.05}$	$6.72^{+15.06}_{-4.96}$	25.22	5.59	$4.1^{+7.0}_{-3.1}$	II	–0.74	–0.37
c2dJ032844.1+312053	3015896	0.1	4.66	0.24	$0.18^{+0.2}_{-0.08}$	$64.38^{+32.72}_{-44.49}$	6.06	0.88	$1.7^{+5.5}_{-0.7}$	II	–1.04	–0.54
c2dJ032846.2+311638	3005111	0.6	1.04	0.23	$0.34^{+0.24}_{-0.14}$	$12.12^{+11.33}_{-6.91}$	41.89	3.27	$1.4^{+2.7}_{-0.4}$	III	–1.31	–0.81
c2dJ032847.8+311655	3017951	3.2	0.69	0.24	$0.21^{+0.15}_{-0.1}$	$3.47^{+8.16}_{-2.98}$	50.54	18.58	$1.3^{+9.8}_{-0.3}$	I	–0.77	–0.37
c2dJ032852.2+312245	3016046	0.5	2.29	0.22	$0.5^{+0.37}_{-0.21}$	$39.73^{+43.16}_{-21.76}$	36.58	2.95	$3.3^{+9.6}_{-2.3}$	II	–0.83	–0.45
c2dJ032856.6+311836	3019661	1.8	4.95	0.24	$0.9^{+1.84}_{-0.77}$	$6.41^{+55.55}_{-5.58}$	592.67	15.96	$1.1^{+0.9}_{-0.1}$	II	–0.3	0.19

Table 2 — *Continued.*

ID_{c2d}	ID_{model}	χ_r^2	A_V	D	$M_\star$	$Age_\star$	$L_\star$	L_{dust}	R_{in}/R_{sub}	Stage	$\alpha_{turnoff}$	α_{excess}
			(mag)	(kpc)	($M_\odot$)	(10^5 yr)	($10^{-2} L_\odot$)	($10^{-2} L_\odot$)				
(1)	(2)	(3)	(4)	(5)	(6)	(7)	(8)	(9)	(10)	(11)	(12)	(13)
c2dJ032857.0+311622	3000710	0.6	7.89	0.24	$0.77^{+0.85}_{-0.65}$	$29.8^{+50.03}_{-27.81}$	58.18	6.79	$62.1^{+43.1}_{-41.4}$	II	0.43	0.97
c2dJ032903.1+312238	3008178	1.7	2.33	0.25	$0.57^{+1.59}_{-0.46}$	$11.51^{+57.65}_{-10.46}$	172.68	4.44	$2.5^{+8.8}_{-1.5}$	II	–0.21	0.26
c2dJ032904.1+305613	3008900	2.5	2.13	0.24	$0.13^{+0.09}_{-0.03}$	$71.02^{+27.2}_{-43.79}$	3.57	0.8	$11.6^{+17.5}_{-10.6}$	II	–0.37	0.29
c2dJ032918.7+312325	3013781	1.8	1.93	0.23	$1.22^{+1.0}_{-0.23}$	$29.04^{+64.13}_{-22.44}$	113.74	16.51	$12.1^{+6.1}_{-4.1}$	II	–0.08	0.09
c2dJ032920.4+311834	3010636	0.8	5.17	0.25	$0.39^{+0.96}_{-0.19}$	$1.33^{+2.53}_{-1.09}$	163.84	150.18	$5.0^{+13.9}_{-4.0}$	I	0.03	0.15
c2dJ032930.4+311903	3006015	0.5	1.01	0.22	$0.25^{+0.33}_{-0.15}$	$34.79^{+44.67}_{-30.14}$	16.3	3.49	$2.6^{+6.3}_{-1.6}$	II	–0.63	–0.22
c2dJ032932.9+312713	3010690	0.7	1.16	0.24	$0.17^{+0.15}_{-0.07}$	$63.83^{+32.0}_{-28.44}$	5.06	0.59	$1.5^{+4.1}_{-0.5}$	II	–1.16	–0.6
c2dJ032937.7+312202	3008900	2.6	2.48	0.24	$0.12^{+0.14}_{-0.02}$	$73.95^{+23.66}_{-70.37}$	3.57	0.83	$3.8^{+38.0}_{-2.8}$	II	–0.56	0.18
c2dJ032954.0+312053	3010241	1.2	3.17	0.22	$0.99^{+0.42}_{-0.44}$	$64.14^{+29.03}_{-48.02}$	44.73	9.72	$2.6^{+17.3}_{-1.6}$	II	–0.02	0.07
c2dJ033024.1+311404	3006161	1.3	0.91	0.25	$0.12^{+0.13}_{-0.02}$	$63.31^{+34.13}_{-34.53}$	6.61	0.64	$5.0^{+8.7}_{-4.0}$	II	–0.75	–0.22
c2dJ033110.7+304941	3010687	1.9	3.45	0.25	$0.85^{+0.63}_{-0.38}$	$59.38^{+30.1}_{-43.95}$	40.35	5.43	$4.5^{+12.1}_{-3.5}$	II	–0.34	–0.27
c2dJ033430.8+311324	3018409	0.2	2.7	0.23	$0.14^{+0.26}_{-0.04}$	$26.83^{+35.33}_{-22.89}$	7.67	1.1	$2.8^{+7.7}_{-1.8}$	II	–0.94	–0.57
c2dJ033449.8+311550	3016746	0.3	1.93	0.23	$0.83^{+0.71}_{-0.4}$	$25.84^{+58.6}_{-16.14}$	48.62	4.7	$1.2^{+1.3}_{-0.2}$	II	–0.91	–0.42
c2dJ034001.5+311017	3016746	0.2	5.0	0.24	$0.35^{+0.63}_{-0.23}$	$59.12^{+39.29}_{-49.83}$	48.62	1.07	$1.3^{+3.5}_{-0.3}$	II	–1.28	–0.76
c2dJ034201.0+314913	3003178	0.1	6.19	0.24	$0.2^{+0.28}_{-0.1}$	$58.81^{+36.99}_{-43.0}$	7.31	1.03	$1.6^{+5.0}_{-0.6}$	II	–1.12	–0.6
c2dJ034204.3+314712	3013699	0.1	5.51	0.23	$0.14^{+0.46}_{-0.04}$	$19.45^{+57.42}_{-16.18}$	15.15	3.18	$1.1^{+9.7}_{-0.1}$	II	–0.71	–0.44
c2dJ034220.3+320531	3017175	0.2	3.5	0.25	$0.51^{+0.32}_{-0.25}$	$67.5^{+29.65}_{-36.31}$	20.97	2.75	$1.2^{+17.7}_{-0.2}$	II	–0.68	–0.17
c2dJ034232.1+315250	3011391	0.5	3.92	0.25	$0.17^{+0.26}_{-0.07}$	$73.52^{+22.22}_{-52.8}$	1.88	0.28	$2.6^{+16.7}_{-1.6}$	II	–1.07	–0.5
c2dJ034249.2+315011	3014019	0.3	4.77	0.23	$0.25^{+0.59}_{-0.14}$	$24.7^{+58.42}_{-21.55}$	19.62	2.9	$1.3^{+3.8}_{-0.3}$	II	–1.2	–0.74
c2dJ034313.7+320045	3009840	1.2	7.33	0.24	$0.37^{+0.71}_{-0.26}$	$51.38^{+33.56}_{-46.53}$	52.12	1.37	$8.5^{+9.5}_{-7.5}$	II	–0.13	0.08
c2dJ034323.6+321226	3010066	0.4	2.54	0.29	$0.18^{+0.22}_{-0.08}$	$61.75^{+35.72}_{-42.78}$	5.67	0.71	$1.4^{+4.4}_{-0.4}$	II	–1.26	–0.59
c2dJ034329.4+315219	3019301	1.9	3.34	0.23	$0.23^{+0.66}_{-0.05}$	$1.41^{+5.52}_{-1.01}$	351.25	19.7	$20.6^{+9.7}_{-3.8}$	II	0.95	0.96
c2dJ034345.2+320359	3018441	0.8	4.83	0.24	$0.23^{+1.2}_{-0.12}$	$0.2^{+3.35}_{-0.18}$	228.28	130.68	$7.9^{+25.6}_{-6.9}$	I	0.65	0.54
c2dJ034348.8+321552	3003975	0.3	1.81	0.26	$0.17^{+0.37}_{-0.07}$	$32.9^{+52.01}_{-28.96}$	8.42	1.38	$5.4^{+9.8}_{-4.4}$	II	–0.71	–0.4
c2dJ034355.3+320753	3013176	0.3	2.46	0.28	$0.15^{+0.2}_{-0.05}$	$50.98^{+46.11}_{-38.41}$	8.72	1.08	$3.2^{+10.3}_{-2.2}$	II	–0.91	–0.41
c2dJ034359.1+321421	3015397	1.6	3.03	0.29	$1.3^{+0.57}_{-0.71}$	$21.07^{+61.0}_{-15.06}$	243.39	8.35	$1.2^{+3.8}_{-0.2}$	II	–0.37	0.03
c2dJ034401.6+322359	3002465	0.3	2.42	0.24	$0.18^{+0.21}_{-0.08}$	$66.82^{+29.88}_{-37.32}$	3.66	0.68	$4.2^{+16.9}_{-3.2}$	II	–0.84	–0.24
c2dJ034402.9+315228	3007428	0.0	5.23	0.25	$0.18^{+0.27}_{-0.07}$	$70.73^{+26.74}_{-56.06}$	3.53	0.42	$1.9^{+9.3}_{-0.9}$	II	–1.06	–0.6
c2dJ034418.2+320457	3006383	1.4	1.87	0.3	$0.39^{+2.47}_{-0.22}$	$2.04^{+52.9}_{-1.55}$	162.9	113.41	$9.2^{+94.7}_{-8.2}$	I	0.14	1.08
c2dJ034425.5+320617	3007450	0.3	5.49	0.28	$0.72^{+0.53}_{-0.39}$	$51.71^{+42.9}_{-34.51}$	100.38	1.99	$9.6^{+33.9}_{-8.6}$	II	–0.43	–0.05
c2dJ034426.0+320430	3014489	1.2	2.79	0.28	$1.09^{+2.38}_{-0.48}$	$4.67^{+70.23}_{-4.03}$	1402.83	224.54	$1.7^{+4.4}_{-0.7}$	I	–0.65	–0.01
c2dJ034427.9+322719	3011356	1.5	2.8	0.23	$0.18^{+0.15}_{-0.08}$	$19.7^{+18.91}_{-17.94}$	34.0	3.89	$2.1^{+5.4}_{-1.1}$	II	–0.78	–0.22
c2dJ034428.5+315954	3003640	0.2	1.36	0.25	$0.22^{+0.27}_{-0.11}$	$19.28^{+27.87}_{-16.15}$	15.25	1.74	$1.5^{+5.4}_{-0.5}$	II	–1.1	–0.47
c2dJ034429.8+320055	3011338	0.4	3.58	0.29	$0.16^{+0.32}_{-0.06}$	$38.8^{+51.83}_{-33.65}$	10.85	1.7	$3.0^{+8.8}_{-2.0}$	II	–0.73	–0.27
c2dJ034432.0+321144	3016117	1.3	6.25	0.33	$2.42^{+1.25}_{-1.78}$	$33.81^{+57.04}_{-29.25}$	7593.6	106.15	$21.7^{+23.3}_{-14.7}$	III	–0.03	–0.17
c2dJ034433.8+315830	3006115	0.5	4.07	0.28	$0.36^{+0.48}_{-0.26}$	$47.97^{+42.66}_{-43.92}$	24.01	5.23	$2.9^{+26.4}_{-1.9}$	II	–0.59	–0.02
c2dJ034435.0+321531	3015526	0.3	2.46	0.26	$0.18^{+0.34}_{-0.07}$	$36.6^{+53.57}_{-31.73}$	9.91	1.01	$3.0^{+7.9}_{-2.0}$	II	–0.52	–0.2
c2dJ034435.5+320856	3013517	1.6	1.92	0.29	$0.2^{+0.39}_{-0.09}$	$0.31^{+2.09}_{-0.29}$	119.01	246.57	$72.9^{+66.6}_{-71.9}$	I	1.37	2.43
c2dJ034437.0+320645	3002420	0.3	2.34	0.22	$1.82^{+0.94}_{-1.29}$	$14.61^{+61.69}_{-10.0}$	1130.45	35.64	$1.7^{+2.4}_{-0.7}$	III	–1.45	–0.82
c2dJ034437.4+320901	3002879	2.5	2.08	0.26	$0.74^{+1.43}_{-0.45}$	$2.62^{+45.67}_{-2.12}$	566.14	131.15	$57.9^{+55.4}_{-56.9}$	I	0.47	0.77
c2dJ034438.0+320330	3008445	1.5	3.98	0.3	$1.23^{+0.57}_{-0.74}$	$28.25^{+66.3}_{-20.24}$	215.36	17.42	$8.0^{+10.1}_{-7.0}$	II	–0.19	0.16
c2dJ034439.8+321804	3003226	0.3	3.51	0.24	$0.49^{+0.67}_{-0.33}$	$32.89^{+56.74}_{-19.7}$	22.26	2.42	$1.7^{+8.1}_{-0.7}$	II	–0.82	–0.24
c2dJ034440.2+320933	3019351	1.7	1.23	0.23	$0.47^{+0.65}_{-0.35}$	$0.47^{+0.95}_{-0.41}$	516.47	412.3	$101.0^{+54.7}_{-100.0}$	I	1.53	1.73
c2dJ034442.6+321002	3005022	1.3	3.16	0.26	$0.18^{+1.39}_{-0.08}$	$1.31^{+83.53}_{-1.01}$	691.28	133.77	$52.8^{+55.8}_{-51.8}$	I	0.57	1.42
c2dJ034443.1+313734	3016867	0.2	6.22	0.24	$0.24^{+0.25}_{-0.13}$	$65.64^{+31.04}_{-44.68}$	5.8	0.5	$1.1^{+36.1}_{-0.1}$	II	–0.75	–0.28
c2dJ034443.8+321030	3014727	1.1	3.24	0.25	$0.16^{+0.1}_{-0.05}$	$6.24^{+11.78}_{-4.98}$	45.58	21.73	$13.3^{+14.1}_{-8.2}$	I	–0.04	0.44
c2dJ034450.4+315236	3007414	0.2	3.46	0.25	$0.16^{+0.33}_{-0.06}$	$77.89^{+19.55}_{-72.68}$	3.63	0.71	$2.9^{+13.4}_{-1.9}$	II	–0.82	–0.18
c2dJ034456.1+320915	3011184	1.4	3.73	0.28	$1.4^{+1.24}_{-0.78}$	$26.49^{+69.04}_{-21.11}$	945.42	46.81	$3.2^{+37.1}_{-2.2}$	II	–0.27	0.53
c2dJ034517.8+321206	3003343	0.5	2.31	0.28	$0.18^{+0.24}_{-0.08}$	$53.74^{+42.09}_{-42.93}$	9.66	1.24	$1.6^{+5.2}_{-0.6}$	II	–1.24	–0.55
c2dJ034529.7+315920	3012232	0.2	4.46	0.25	$0.18^{+0.18}_{-0.07}$	$79.08^{+18.53}_{-35.38}$	3.63	0.54	$5.6^{+21.3}_{-4.6}$	II	–0.82	–0.25

Table 2 — *Continued.*

$\mathrm{ID_{c2d}}$	$\mathrm{ID_{model}}$	χ^2_r	A_V	D	$M_\star$	Age$_\star$	$L_\star$	$L_{\rm dust}$	$R_{\rm in}/R_{\rm sub}$	Stage	$\alpha_{\rm turnoff}$	$\alpha_{\rm excess}$
			(mag)	(kpc)	($M_\odot$)	(10^5 yr)	($10^{-2}L_\odot$)	($10^{-2}L_\odot$)				
(1)	(2)	(3)	(4)	(5)	(6)	(7)	(8)	(9)	(10)	(11)	(12)	(13)
c2dJ034533.5+314555	3010281	0.1	5.97	0.25	$0.16^{+0.3}_{-0.06}$	$79.23^{+18.37}_{-56.63}$	3.49	0.41	$3.4^{+17.2}_{-2.4}$	II	–0.84	–0.34
c2dJ034535.6+315954	3018513	0.1	5.1	0.24	$0.24^{+0.39}_{-0.13}$	$44.58^{+48.99}_{-39.23}$	13.93	1.08	$4.4^{+16.0}_{-3.4}$	II	–0.73	–0.22
c2dJ034657.4+324917	3000062	0.1	2.52	0.24	$0.19^{+0.22}_{-0.08}$	$64.34^{+32.75}_{-42.38}$	5.7	1.0	$1.5^{+4.3}_{-0.5}$	II	–1.14	–0.47
IR2 band turnoff												
c2dJ032851.1+311632	3009474	0.7	1.75	0.24	$0.16^{+0.15}_{-0.06}$	$54.6^{+36.54}_{-31.98}$	7.84	0.5	$1.5^{+4.1}_{-0.5}$	II	–1.16	–0.76
c2dJ032852.2+311547	3013176	0.8	2.88	0.24	$0.14^{+0.11}_{-0.03}$	$37.52^{+25.86}_{-31.7}$	8.72	0.84	$2.1^{+7.5}_{-1.1}$	II	–1.04	–0.82
c2dJ032852.9+311626	3019740	0.7	1.81	0.25	$0.17^{+0.15}_{-0.06}$	$70.91^{+26.7}_{-33.59}$	3.79	0.38	$1.5^{+4.8}_{-0.5}$	II	–0.43	0.22
c2dJ032909.5+312721	3006161	0.1	4.07	0.24	$0.19^{+0.21}_{-0.09}$	$72.04^{+25.06}_{-46.23}$	6.61	0.84	$10.9^{+10.2}_{-9.9}$	II	–0.54	–0.34
c2dJ032917.8+311948	3014115	0.1	5.88	0.25	$0.18^{+0.19}_{-0.07}$	$72.46^{+25.01}_{-48.93}$	5.91	0.76	$2.8^{+13.0}_{-1.8}$	II	–0.71	–0.38
c2dJ032921.6+312110	3018513	1.0	1.81	0.23	$0.3^{+0.26}_{-0.19}$	$43.7^{+48.98}_{-30.16}$	13.93	0.99	$3.4^{+15.4}_{-2.4}$	II	–0.76	–0.25
c2dJ032923.2+312653	3000123	0.6	2.21	0.24	$0.14^{+0.18}_{-0.04}$	$41.76^{+38.53}_{-37.62}$	34.54	0.8	$2.2^{+8.4}_{-1.2}$	II	–0.26	0.22
c2dJ032928.9+305842	3008430	1.3	0.62	0.25	$0.13^{+0.21}_{-0.03}$	$48.8^{+35.62}_{-42.55}$	4.97	0.66	$19.1^{+11.7}_{-8.2}$	II	–0.26	0.14
c2dJ032929.8+312103	3005493	0.3	1.91	0.23	$0.14^{+0.23}_{-0.04}$	$16.81^{+34.57}_{-13.88}$	22.63	2.38	$9.2^{+14.9}_{-8.2}$	II	–0.45	–0.16
c2dJ032937.6+310249	3008677	0.2	1.69	0.26	$0.1^{+0.17}_{-0.0}$	$91.2^{+3.96}_{-32.9}$	1.5	0.14	$8.3^{+17.8}_{-7.3}$	II	–0.77	–0.26
c2dJ033120.1+304918	3000664	0.4	3.05	0.25	$0.12^{+0.22}_{-0.02}$	$35.59^{+42.75}_{-34.47}$	52.32	4.94	$4.1^{+12.3}_{-3.1}$	I	–0.21	0.28
c2dJ033346.9+305350	3014115	0.5	1.83	0.25	$0.16^{+0.13}_{-0.06}$	$71.56^{+26.04}_{-32.6}$	5.91	0.72	$2.8^{+13.5}_{-1.8}$	II	–0.59	–0.01
c2dJ034336.0+315009	3004647	1.3	0.7	0.22	$0.3^{+0.65}_{-0.07}$	$14.73^{+41.19}_{-7.96}$	19.78	1.32	$16.8^{+108.3}_{-15.8}$	II	0.2	0.66
c2dJ034346.5+321106	3018345	0.2	3.4	0.33	$0.14^{+0.2}_{-0.04}$	$83.29^{+15.22}_{-55.22}$	2.63	0.19	$3.2^{+17.9}_{-2.2}$	II	0.15	0.72
c2dJ034347.6+320903	3008677	0.4	3.21	0.32	$0.13^{+0.12}_{-0.03}$	$83.55^{+14.67}_{-34.86}$	1.5	0.16	$5.3^{+15.7}_{-4.3}$	II	–0.59	–0.24
c2dJ034415.8+315937	3019728	0.2	2.9	0.28	$0.17^{+0.17}_{-0.07}$	$67.5^{+30.1}_{-50.52}$	4.18	0.49	$11.2^{+17.9}_{-10.2}$	II	–0.4	0.04
c2dJ034421.3+321156	3004577	0.5	2.71	0.26	$0.48^{+0.41}_{-0.26}$	$54.12^{+40.45}_{-31.05}$	14.56	1.23	$4.5^{+11.9}_{-3.5}$	II	0.01	0.14
c2dJ034427.2+322029	3019764	0.3	2.28	0.29	$0.18^{+0.24}_{-0.08}$	$64.37^{+33.07}_{-40.1}$	7.72	0.68	$3.5^{+17.5}_{-2.5}$	II	–0.82	–0.27
c2dJ034430.8+320956	3020088	1.1	2.38	0.33	$2.16^{+0.49}_{-0.33}$	$60.88^{+15.57}_{-18.89}$	4537.84	18.11	$41.0^{+20.6}_{-24.4}$	III	0.02	0.01
c2dJ034658.5+324659	3002972	0.4	3.17	0.24	$0.21^{+0.22}_{-0.1}$	$56.68^{+39.12}_{-39.94}$	5.56	0.52	$1.7^{+5.4}_{-0.7}$	II	–1.16	–0.65
IR3 band turnoff												
c2dJ032858.1+311804	3011544	0.3	2.56	0.25	$0.48^{+0.26}_{-0.17}$	$69.2^{+28.95}_{-35.51}$	19.21	0.2	$55.8^{+886.5}_{-54.8}$	III	–1.97	–1.38
c2dJ032908.0+312251	3019657	1.0	3.08	0.23	$0.44^{+1.21}_{-0.3}$	$0.7^{+3.88}_{-0.65}$	625.91	216.22	$52.4^{+40.5}_{-33.3}$	I	1.52	1.86
c2dJ032912.9+312329	3011599	1.9	0.48	0.23	$0.19^{+0.12}_{-0.06}$	$0.81^{+1.59}_{-0.14}$	55.98	26.53	$72.1^{+16.5}_{-9.4}$	I	1.6	2.17
c2dJ032916.8+312325	3000622	2.3	2.16	0.23	$0.78^{+1.53}_{-0.62}$	$0.15^{+96.33}_{-0.13}$	33.61	2.46	$11.4^{+32.8}_{-10.4}$	II	0.6	1.04
c2dJ032926.8+312648	3015385	3.5	1.64	0.22	$0.59^{+0.84}_{-0.11}$	$18.13^{+61.17}_{-3.32}$	75.58	0.75	$615.6^{+1618.4}_{-422.5}$	II	–1.06	–0.02
c2dJ032929.3+311835	3015686	1.7	3.48	0.25	$0.53^{+0.51}_{-0.07}$	$30.84^{+68.48}_{-10.9}$	35.7	7.53	$213.6^{+129.2}_{-122.1}$	II	1.16	1.26
c2dJ034233.1+315215	3014024	0.2	4.67	0.24	$0.11^{+0.2}_{-0.01}$	$71.51^{+25.59}_{-45.7}$	14.75	0.36	$21.0^{+32.7}_{-20.0}$	II	–0.02	0.45
c2dJ034234.2+315101	3003543	0.1	3.79	0.23	$0.12^{+0.14}_{-0.01}$	$79.74^{+20.05}_{-38.41}$	3.43	0.24	$55.7^{+52.5}_{-30.8}$	II	0.27	0.85
c2dJ034250.9+314045	3005351	0.4	5.92	0.24	$0.27^{+0.4}_{-0.17}$	$51.31^{+46.16}_{-43.19}$	13.01	0.22	$44.8^{+265.4}_{-43.8}$	II	–1.14	0.47
c2dJ034301.9+314436	3016352	2.7	4.22	0.25	$0.13^{+0.19}_{-0.01}$	$11.99^{+14.19}_{-7.77}$	10.12	1.14	$28.8^{+93.3}_{-27.7}$	I	0.75	1.55
c2dJ034308.7+315139	3002609	1.8	3.71	0.22	$0.28^{+0.09}_{-0.17}$	$2.65^{+64.54}_{-2.1}$	11.87	1.18	$72.4^{+69.0}_{-24.1}$	II	1.53	2.11
c2dJ034344.6+320818	3018287	0.8	2.42	0.25	$0.82^{+0.96}_{-0.32}$	$52.04^{+27.79}_{-49.88}$	72.61	2.56	$79.9^{+297.5}_{-78.2}$	II	0.85	1.75
c2dJ034410.1+320405	3018669	1.5	1.5	0.32	$0.16^{+0.29}_{-0.06}$	$0.1^{+1.21}_{-0.07}$	76.01	118.91	$73.8^{+65.8}_{-72.0}$	I	1.5	1.63
c2dJ034415.2+321942	3015752	1.4	3.47	0.31	$0.2^{+0.67}_{-0.09}$	$40.65^{+30.57}_{-17.14}$	8.3	1.98	$43.2^{+98.3}_{-17.7}$	II	0.81	1.23
c2dJ034418.2+320959	3005606	0.5	3.73	0.26	$0.24^{+0.25}_{-0.13}$	$34.14^{+58.68}_{-29.1}$	19.59	1.02	$14.3^{+49.7}_{-13.3}$	II	–0.54	0.09
c2dJ034422.3+320543	3009294	0.7	2.09	0.21	$1.0^{+1.01}_{-0.51}$	$10.57^{+16.26}_{-1.17}$	162.02	5.49	$41.5^{+17.8}_{-17.5}$	II	0.46	0.54
c2dJ034422.6+320154	3004647	0.7	1.96	0.25	$0.25^{+0.37}_{-0.14}$	$20.3^{+44.1}_{-18.27}$	19.78	1.92	$99.5^{+84.7}_{-55.7}$	II	0.87	1.87
c2dJ034425.7+321549	3009409	2.0	1.1	0.28	$0.15^{+0.59}_{-0.04}$	$0.93^{+66.26}_{-0.9}$	33.92	19.34	$65.7^{+75.7}_{-64.7}$	I	1.71	2.21
c2dJ034429.2+320116	3002365	0.4	7.04	0.28	$0.34^{+0.54}_{-0.24}$	$44.01^{+49.91}_{-38.97}$	16.92	0.4	$44.4^{+61.9}_{-43.4}$	II	0.2	1.04
c2dJ034429.7+321040	3002351	1.5	1.42	0.29	$0.59^{+0.98}_{-0.08}$	$5.42^{+7.4}_{-0.4}$	198.15	11.22	$27.1^{+32.2}_{-4.3}$	II	0.5	0.76
c2dJ034434.1+321636	3014280	0.1	3.27	0.28	$0.19^{+0.4}_{-0.09}$	$63.79^{+33.36}_{-52.24}$	16.02	0.38	$3.4^{+11.3}_{-2.4}$	II	0.09	0.63
c2dJ034434.8+315655	3007580	1.5	2.26	0.25	$0.29^{+0.29}_{-0.19}$	$42.37^{+42.76}_{-37.53}$	19.76	0.61	$1.3^{+86.6}_{-0.3}$	II	0.11	1.26
c2dJ034437.4+321224	3000393	0.5	6.22	0.3	$0.92^{+0.57}_{-0.7}$	$42.8^{+37.03}_{-31.37}$	189.15	5.21	$52.9^{+42.3}_{-26.2}$	II	0.56	0.93
c2dJ034438.0+321137	3003770	0.8	0.9	0.25	$0.21^{+0.06}_{-0.09}$	$4.94^{+36.18}_{-3.54}$	40.14	4.68	$46.0^{+32.6}_{-22.9}$	II	0.91	1.7
c2dJ034439.0+320320	3015863	4.2	1.27	0.32	$0.13^{+0.15}_{-0.03}$	$0.05^{+1.26}_{-0.02}$	64.66	31.03	$57.3^{+49.0}_{-4.7}$	I	2.15	2.06

Table 2 — *Continued.*

ID_{c2d}	ID_{model}	χ_r^2	A_V	D	$M_\star$	$Age_\star$	$L_\star$	L_{dust}	R_{in}/R_{sub}	Stage	$\alpha_{turnoff}$	α_{excess}
			(mag)	(kpc)	($M_\odot$)	(10^5 yr)	($10^{-2} L_\odot$)	($10^{-2} L_\odot$)				
(1)	(2)	(3)	(4)	(5)	(6)	(7)	(8)	(9)	(10)	(11)	(12)	(13)
c2dJ034439.2+322009	3003660	1.5	2.25	0.3	$0.13^{+0.09}_{-0.03}$	$5.46^{+13.76}_{-4.45}$	18.89	8.56	$61.9^{+61.0}_{-22.7}$	II	1.23	1.71
c2dJ034441.7+321202	3004538	1.4	4.54	0.26	$0.32^{+0.92}_{-0.21}$	$29.6^{+59.14}_{-27.56}$	26.64	14.13	$94.0^{+114.1}_{-68.4}$	II	0.27	1.32
c2dJ034442.6+320619	3000760	1.2	1.1	0.32	$0.63^{+0.62}_{-0.17}$	$68.52^{+20.32}_{-67.99}$	24.63	5.15	$79.0^{+137.0}_{-35.6}$	II	1.39	2.32
c2dJ034443.0+321560	3010384	1.1	1.9	0.29	$0.19^{+0.06}_{-0.08}$	$1.17^{+1.22}_{-0.67}$	68.55	23.57	$38.5^{+50.2}_{-0.9}$	I	0.71	0.7
c2dJ034444.6+320813	3006152	1.4	0.76	0.32	$0.2^{+0.23}_{-0.1}$	$0.5^{+2.69}_{-0.48}$	199.18	127.76	$32.3^{+39.8}_{-31.3}$	I	1.24	1.85
c2dJ034457.9+320402	3010073	0.6	1.86	0.28	$0.16^{+0.15}_{-0.06}$	$50.83^{+40.66}_{-41.65}$	7.9	0.29	$2.4^{+16.0}_{-1.4}$	II	–1.35	–1.07
c2dJ034460.0+322233	3018345	0.1	2.53	0.25	$0.13^{+0.21}_{-0.03}$	$87.96^{+10.55}_{-39.16}$	2.63	0.2	$7.9^{+21.2}_{-6.9}$	II	–0.34	0.04
c2dJ034501.4+320502	3016376	1.3	0.7	0.3	$1.23^{+0.62}_{-0.38}$	$43.77^{+54.38}_{-32.22}$	145.22	2.14	$6.1^{+39.2}_{-5.1}$	III	–1.81	–0.92
c2dJ034504.7+321501	3001936	0.7	4.02	0.27	$0.24^{+0.62}_{-0.14}$	$33.12^{+61.54}_{-30.23}$	8.6	0.45	$106.0^{+443.6}_{-70.2}$	II	–0.04	1.44
c2dJ034513.5+322435	3018104	0.5	3.17	0.24	$0.16^{+0.35}_{-0.06}$	$70.84^{+26.59}_{-66.73}$	10.69	0.26	$1.9^{+7.1}_{-0.9}$	II	–0.54	–0.07
IR4 band turnoff												
c2dJ032854.1+311654	3012867	0.7	6.86	0.24	$0.86^{+1.21}_{-0.7}$	$24.61^{+70.31}_{-23.57}$	98.6	38.52	$2.4^{+4.8}_{-1.4}$	II	–0.72	0.38
c2dJ033027.1+302830	3009118	1.9	1.61	0.27	$0.2^{+0.98}_{-0.05}$	$1.2^{+6.0}_{-0.46}$	339.8	31.42	$126.4^{+76.6}_{-125.4}$	I	2.76	2.76
c2dJ034227.1+314433	3007649	0.6	6.88	0.25	$0.8^{+0.28}_{-0.38}$	$64.48^{+30.97}_{-48.89}$	47.89	1.45	$267.1^{+244.8}_{-116.8}$	II	1.17	2.1
c2dJ034254.7+314345	3009555	0.4	1.41	0.23	$0.71^{+0.51}_{-0.25}$	$55.53^{+43.05}_{-37.56}$	27.91	0.5	$67.9^{+92.3}_{-33.6}$	II	0.13	0.93
c2dJ034306.8+314821	3012886	0.4	2.67	0.23	$0.21^{+0.27}_{-0.09}$	$17.06^{+20.52}_{-14.54}$	24.52	0.77	$157.9^{+794.5}_{-121.7}$	II	0.2	1.17
c2dJ034419.1+320931	3010204	1.2	0.31	0.33	$1.58^{+0.09}_{-0.08}$	$66.66^{+32.79}_{-13.64}$	211.55	0.74	$6.5^{+5.2}_{-5.5}$	III	–1.84	–1.45
c2dJ034421.6+321510	3009308	2.6	0.7	0.3	$0.14^{+0.14}_{-0.04}$	$33.21^{+22.18}_{-29.78}$	10.0	2.49	$175.4^{+2655.6}_{-147.8}$	II	–0.18	1.57
c2dJ034431.5+320845	3005300	2.0	1.63	0.29	$1.27^{+0.58}_{-0.55}$	$26.79^{+51.42}_{-11.74}$	186.0	37.17	$194.2^{+53.9}_{-42.8}$	II	2.75	2.89
c2dJ034456.8+315411	3019546	0.5	2.29	0.25	$0.14^{+0.1}_{-0.03}$	$79.92^{+13.93}_{-24.53}$	4.16	0.1	$49.2^{+174.4}_{-48.2}$	II	–0.01	0.97
c2dJ034507.6+321028	3018977	0.9	0.34	0.29	$1.31^{+0.4}_{-0.29}$	$38.55^{+59.59}_{-27.0}$	215.43	1.21	$3.3^{+15.0}_{-2.3}$	III	–2.1	–1.51
W3 band turnoff												
c2dJ032916.7+311618	3015991	0.7	0.8	0.22	$0.27^{+0.26}_{-0.11}$	$20.12^{+18.71}_{-12.41}$	23.09	0.04	$76.1^{+2504.9}_{-75.1}$	II	–1.55	0.86
c2dJ033026.0+310218	3018696	0.8	2.07	0.22	$1.0^{+0.78}_{-0.61}$	$18.79^{+65.97}_{-9.66}$	63.75	0.26	$7.1^{+1335.9}_{-6.1}$	III	–1.79	–0.58
c2dJ033351.1+311228	3008112	1.1	2.71	0.22	$0.24^{+0.08}_{-0.07}$	$8.24^{+7.82}_{-4.11}$	26.78	1.09	$795.5^{+1649.5}_{-752.3}$	II	–0.83	0.75
c2dJ034011.8+315523	3010915	1.7	3.57	0.25	$0.51^{+0.3}_{-0.15}$	$48.64^{+48.16}_{-47.47}$	24.27	1.29	$835.7^{+61.4}_{-834.7}$	II	4.14	8.04

Notes: (1): c2d ID;

(2): ID of the Best-fit model from Robitaille et al. (2006);

(3): Minimum reduced χ^2;

(4): The most probable V-band interstellar extinction;

(5): The most probable heliocentric distance;

(6): The most probable stellar mass and the 95% confidence interval;

(7): The most probable stellar age and the 95% confidence interval;

(8): The best-fit stellar bolometric luminosity;

(9): Dust luminosity from integral of the model SED of disk+envelope that best fits the observed SED;

(10): The disk inner radius, in units of the dust sublimation radius, and the 95% confidence interval;

(11): Evolutionary stage;

(12): Spectral indices at $\lambda > \lambda_{\rm turnoff}$ for stellar photosphere-included IR SEDs.

(13): Spectral indices at $\lambda > \lambda_{\rm turnoff}$ for stellar photosphere-subtracted IR SEDs.

4.2.1 Stellar mass distribution of the central stellar sources

The histogram of stellar masses of YSOs in our sample is shown in the left panel of Figure 5. As pointed out above, our sample is expected to be statistically unbiased at $M_\star \gtrsim 0.9\ M_\odot$. We overplot the Salpeter stellar initial mass function (IMF; Salpeter 1955) which was scaled to have the same number of stars at $M_\star >0.9\ M_\odot$ as our YSO sample. The error bars in the histogram represent the Poisson noise from number counts. It can be seen that the mass distribution of our YSOs at $M_\star \gtrsim 1\ M_\odot$ is consistent with the Salpeter IMF within the uncertainties. Note that an extended star formation history for the Perseus region might make it not straightforward to compare

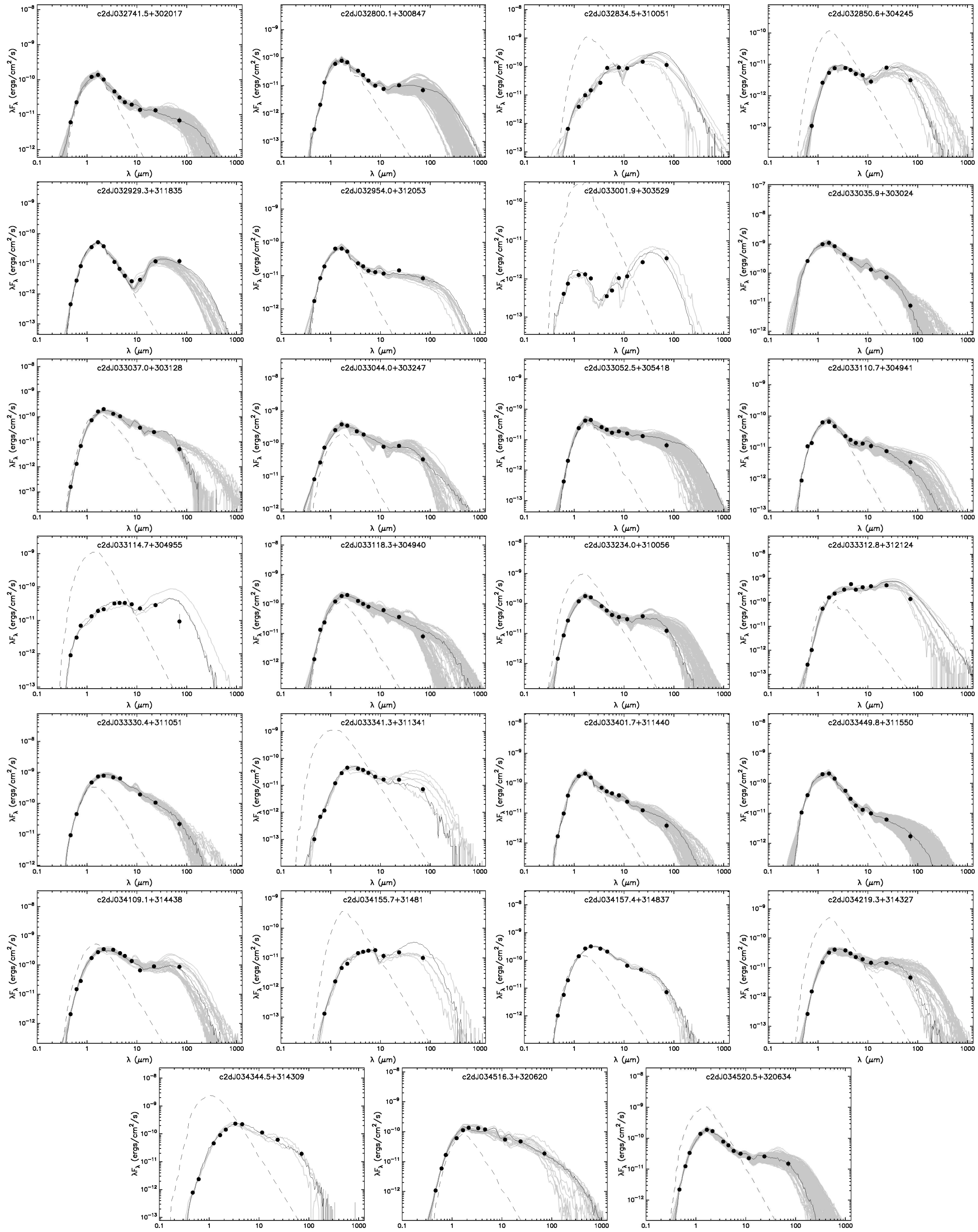

Fig. 4 SEDs of 27 Perseus YSOs. Among our whole sample, these YSOs have at least one optical band, JHK_s, IRAC or WISE, MIPS 24 μm or WISE 22 μm, and MIPS 70 μm available (*black points*). The black solid curve in each panel represents the best-fit model SED of Robitaille et al. (2007), and the grey curves represent all subsequent well-fit models with $\chi^2_{\rm r} - \chi^2_{\rm r,best} < 2$. The dashed lines illustrate the SEDs of the stellar photosphere in the best-fit model, as it would appear to be without circumstellar dust.

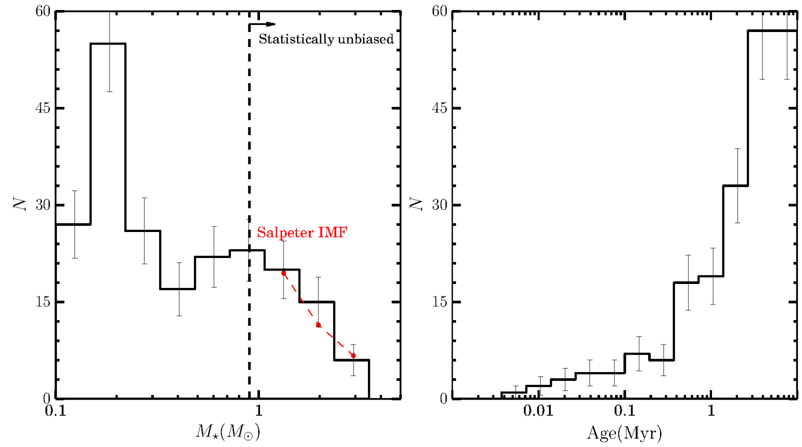

Fig. 5 Histograms of the stellar masses (*left*) and ages (*right*) for the whole sample of YSOs. The filled red circles in the left panel represent the Salpeter IMF which is scaled to have the same number of observed stars more massive than 0.9 $M_\odot$.

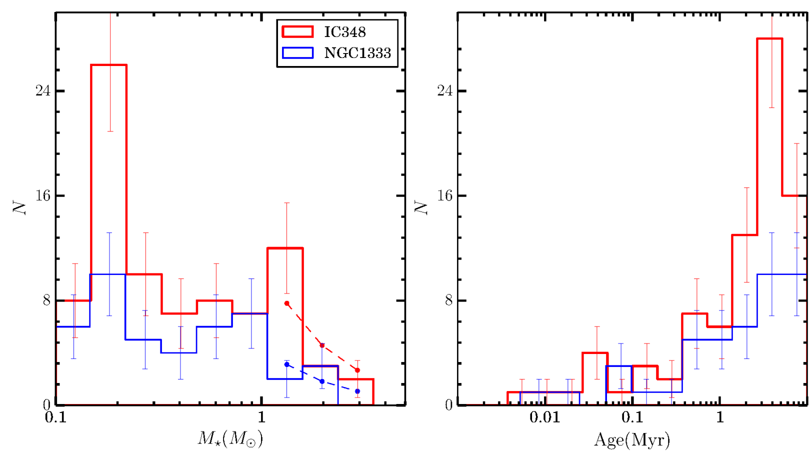

Fig. 6 Histograms of the stellar masses (*left*) and ages (*right*) for the two major clusters IC 348 (*thick red*) and NGC 1333 (*thin blue*). YSOs within a 15′ radius of each of the two clusters are regarded as being associated with the cluster. The filled red (*blue*) circles in the left panel represent the Salpeter IMF for IC 348 (NGC 1333) that is scaled to have the same number of observed stars more massive than 0.9 $M_\odot$.

the accumulated present-day mass function with the simple Salpeter IMF. Although our sample may be subjected to significant incompleteness bias below 1 $M_\odot$, we note that a flat and broad mass distribution from sub-solar to the sub-stellar mass limit, as found in our sample, is in general agreement with previous studies on low-mass clusters such as IC 348 (e.g. Luhman et al. 2003a; Muench et al. 2003), NGC 1333 (e.g. Wilking et al. 2004; Greissl et al. 2007), Trapezium (e.g. Muench et al. 2002) and other nearby clusters (e.g. Andersen et al. 2008; Hillenbrand & Carpenter 2000; Luhman et al. 2000; Lucas et al. 2005; Luhman 2007; Levine et al. 2006; Moraux et al.

2003; Slesnick et al. 2004; Scholz et al. 2009; Weights et al. 2009). The median $M_\star$ of our YSOs is $\simeq 0.3\,M_\odot$. Stellar mass distributions of YSOs within a 15′ radius of each of the two major clusters IC 348 and NGC 1333 are shown in the left panel of Figure 6. The median stellar masses of YSOs in IC 348 and NGC 1333 are $\simeq$ 0.3 $M_\odot$.

4.2.2 *Age distribution of the central stellar sources*

The age histogram for the whole sample is shown in the right panel of Figure 5, and the age histograms for each of the two major clusters (again defined with a 15′ radius) are shown in the right panel of Figure 6. The median stellar age of the whole sample is $\simeq$3.1 Myr, and the median age for YSOs in IC 348 and NGC 1333 is $\simeq$ 2.8 and 2.5 Myr respectively. A relatively younger age of NGC 1333 than IC 348 is in line with previous studies, and our age estimate is consistent with previous studies of YSOs in these two clusters (e.g. Herbig 1998; Luhman et al. 2003b; Lada et al. 2006; Winston et al. 2009).

4.2.3 *Uncertainties in stellar parameters from SED modeling*

Determination of the masses and ages of central stellar sources relies on a reasonably accurate constraint on the effective temperature $T_{\rm eff}$. While it is reasonable to statistically explore the distribution of masses and ages determined from broadband SED modeling for a large sample, results for individual sources may be subject to large uncertainties. In principle, $T_{\rm eff}$ can be accurately constrained by photospheric absorption lines from optical or near-IR spectroscopy. By comparing our SED-based and the spectroscopy-based $T_{\rm eff}$ for 75 IC 348 YSOs that have spectroscopic observations in the literature (e.g. Luhman et al. 2003b; Lada et al. 2006; Muzerolle et al. 2006; Muench et al. 2007), we found a median and standard deviation of $T_{\rm eff,SED}-T_{\rm eff,Spec}$ of 71 ($\sim$ 2%) and 257 K ($\sim$ 7%) respectively for the 35 objects with A_V <4 mag and $T_{\rm eff,Spec}$ <5000 K, and a median and standard deviation of $T_{\rm eff,SED}-T_{\rm eff,Spec}$ of 68 ($\sim$ 2%) and 434 K ($\sim$ 12%) respectively for the 31 objects with A_V >4 mag and $T_{\rm eff,Spec}$ <5000 K. In addition, the remaining nine objects with $T_{\rm eff,Spec}$ >5000 K have a median and standard deviation of $T_{\rm eff,SED}-T_{\rm eff,Spec}$ of -1333 ($\sim$ 24%) and 1229 K ($\sim$ 16%) respectively. According to the theoretical evolutionary tracks of Baraffe et al. (1998), for a PMS star with $T_{\rm eff}$ of 3336 K and an age of 3 Myr, which corresponds to a stellar mass of 0.3 $M_\odot$, an overestimation of $T_{\rm eff}$ by $\sim$350 K ($\sim$2–3 subclasses in spectral type) at a given luminosity can result in an overestimation of age and mass by factors of 3 and 2 respectively.

4.2.4 *Evolutionary stages of YSOs*

Similar to Povich et al. (2013), for every YSO, we calculated the accumulated probability ($P_{\rm stage}\propto\sum_{\rm model\ i}$ e$^{-\chi^2_{\rm i,r}/2}$) of it being in each of the three Stages (i.e. $P_{\rm StageI}$, $P_{\rm StageII}$, $P_{\rm StageIII}$) based on all the well-fit models with $\chi^2_{\rm r} - \chi^2_{\rm r,best} < 2$. A YSO is uniquely classified as a Stage I, II or III object if the normalized $P_{\rm Stage} > 0.67$. The result of our classification is presented in Figure 7. There are 5% of YSOs that cannot be classified as either Stage I, II or III if the 0.67 probability threshold is adopted. These 5% of objects were classified as evolutionary stages that have the highest accumulated probability. The classification of some YSOs into the Stage I phase may be subject to relatively large uncertainties. This is because the wavelength coverage of our SEDs is mostly limited to $\lesssim$ 24 μm, shortward of which the contribution of excess emission from disks dominates over that from the cool infalling envelopes. Moreover, we note that some of our Stage I YSOs with low IR excess luminosities may be genuine Stage II YSOs with edge-on optically thick disks.

As can be seen from Figure 7, our sample is dominated by Stage II YSOs. Moreover, the fractions of YSOs in different stages are similar for IC 348, NGC 1333 and the other regions. As men-

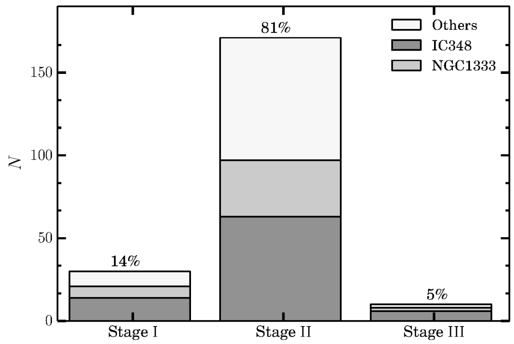

Fig. 7 Classification of evolutionary stages of our sample based on the fractional envelope accretion rates and disk masses.

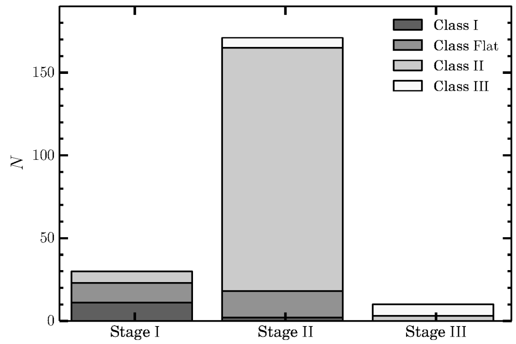

Fig. 8 Breakdown of different evolutionary stages into different $\alpha(K_s-\mathrm{M1})$–based Classes.

tioned in the Introduction section, YSOs have been historically grouped into three or four classes based on the spectral index α determined over the wavelength range from $\sim$ 2 to 20 μm. YSOs from different classes are thought to be in different evolutionary stages (see above for references). R06 showed that there is a general correspondence between the modeling-based "Stages" and α-based "Classes," in the sense that Stage I is expected to include the Class 0/I, Stage II is analogous to Class II and Stage III to Class III. However, as a set of purely empirical criteria, the Class scheme can be sometimes misleading.

Figure 8 presents the breakdown of each Stage into different Classes. As is shown, a vast majority (94%) of Class II objects are grouped into the Stage II, and the majority (85%) of Class I objects are grouped into the Stage I. It is noteworthy that the dominant physical Stages for Class FLAT YSOs are uncertain, with about 43% being in Stage I and the remaining 57% in Stage II. Likewise, the dominant physical Stages for Class III YSOs are also uncertain, with about 46% of them being in Stage II and the remaining 54% in Stage III.

5 PROPERTIES OF THE CIRCUMSTELLAR DISKS

The near- to mid-IR excesses that are emitted above the stellar photosphere can be used to probe properties of the disk, such as the disk luminosity (basically an integral of the IR excesses) and disk geometry (e.g. Dullemond et al. 2007; Espaillat et al. 2013; Hughes et al. 2010; Kim et al. 2009; Merín et al. 2010). In particular, disk flaring (e.g. Kenyon & Hartmann 1987) and radius of the inner disk edge are the two primary parameters of disk geometry that shape the SED of IR excesses. As the disk evolves, dust grains in the inner circumstellar disks may gradually settle down (e.g. Dullemond & Dominik 2005) or be cleared out dynamically (Lubow & D'Angelo 2006) or through photoevaporation (Alexander et al. 2006a), which leads to a progressive suppression of emission excesses from near- to mid-IR wavelengths. Features of the IR SEDs that are closely related to the disk clearing and flaring include the longest measured wavelength $\lambda_{\rm turnoff}$ shortward of which the emission is consistent with being purely from the stellar photosphere, and the spectral index $\alpha_{\rm excess}$ at $\lambda > \lambda_{\rm turnoff}$ (e.g. Cieza et al. 2007; Harvey et al. 2007; Merín et al. 2008).

5.1 $\alpha_{\rm excess}$ vs. $\lambda_{\rm turnoff}$

$\lambda_{\rm turnoff}$ is closely related to the physical scales of the inward disk truncation or clearing radius (e.g. Calvet et al. 2002; Rice et al. 2003), and $\alpha_{\rm excess}$ is related to both the inward disk clearing and disk flaring which in turn affect the disk temperature gradients. In particular, for an optically thick disk,

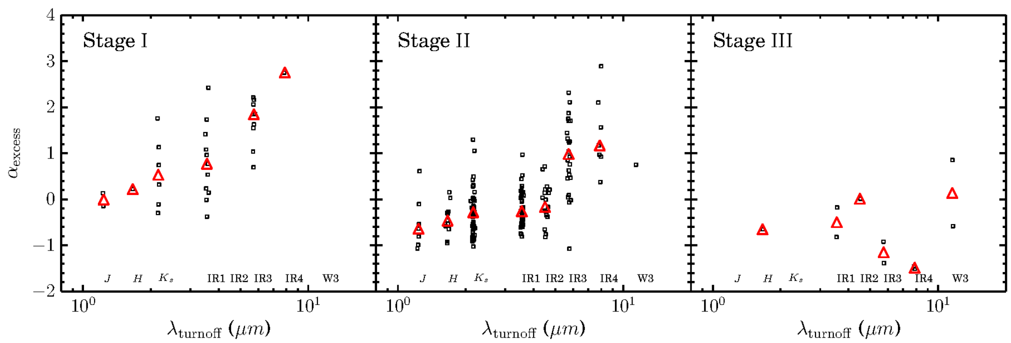

Fig. 9 Distribution of $\alpha_{\rm excess}$ vs. the wavelength bands $\lambda_{\rm turnoff}$ longward of which IR excesses are observed. YSOs in Stages I, II and III are shown separately in the *left*, *middle* and *right* panels. The median of $\alpha_{\rm excess}$ at each individual $\lambda_{\rm turnoff}$ for different Stages is shown as red triangles. Note that data points at a given wavelength band are slightly shifted randomly in the horizontal direction for clarity. See the text for details.

a larger spectral index corresponds to a shallower temperature gradient (e.g. Beckwith et al. 1990). By comparing the observed SED of each YSO with the best-fit emergent stellar fluxes (which are corrected for interstellar extinction), we determined the turnoff wavelength band $\lambda_{\rm turnoff}$, longward of which $\geq 3\sigma$ excesses above the stellar photosphere level were observed, and calculated $\alpha_{\rm excess}$ for wavelength ranges longward of $\lambda_{\rm turnoff}$. Previous studies of YSO IR spectral indices did not exclude the contribution of direct stellar photosphere emission. In this work, we focus on $\alpha_{\rm excess}$ determined for the photosphere-subtracted IR SEDs in order to investigate properties of the disk.

In Table 2 we list spectral indices determined for both the photosphere-included SEDs ($\alpha_{\rm turnoff}$) and photosphere-subtracted SEDs ($\alpha_{\rm excess}$) at $\lambda \geq \lambda_{\rm turnoff}$. The distributions on the $\lambda_{\rm turnoff}$ vs. $\alpha_{\rm excess}$ diagram for the subsamples from Stage I, II and III YSOs are shown separately in Figure 9.

The median $\alpha_{\rm excess}$ at each $\lambda_{\rm turnoff}$ is also indicated as red triangles in Figure 9. The majority of Stage I YSOs have $\alpha_{\rm excess} \gtrsim 0.0$, whereas the majority of Stage III YSOs have $\alpha_{\rm excess} \lesssim 0.0$. Compared to the Stage I and III YSOs, the Stage II YSOs have a larger range of $\alpha_{\rm excess}$ from ~ -1 to 3. The median $\alpha_{\rm excess}$ gradually increases with increasing $\lambda_{\rm turnoff}$ for both Stage I and II YSOs. No obvious trend in the median $\alpha_{\rm excess}$ with $\lambda_{\rm turnoff}$ is found for the Stage III YSOs. In addition, there is a hint that the standard deviation of $\alpha_{\rm excess}$ increases with increasing $\lambda_{\rm turnoff}$ for the Stage II YSOs which have the largest sample size. In particular, the standard deviations of $\alpha_{\rm excess}$ for the Stage II YSOs with different turnoff wavelengths at $\lambda_{\rm turnoff} \leq$ IR2 and $\geq$ IR3 are $\sim$ 0.4 and 0.8 respectively. A smaller spread of $\alpha_{\rm turnoff}$ at shorter $\lambda_{\rm turnoff}$ has been observed before (e.g. Cieza et al. 2007, Merín et al. 2008). Cieza et al. (2007) found that all the known Classical T Tauri stars (CTTs), which are defined by having relatively strong nebular emission lines and thus are actively accreting, cluster around $\alpha_{\rm turnoff} \sim -1.0$ and $\lambda_{\rm turnoff} \lesssim K_s$, whereas the Weak-line T Tauri stars (WTTs) exhibit a much larger spread in $\alpha_{\rm turnoff}$ and $\lambda_{\rm turnoff}$.

5.2 Fractional Dust Luminosity vs. $\lambda_{\rm turnoff}$

The ratio of the circumstellar dust luminosity $L_{\rm dust}$ to stellar luminosity $L_\star$, which is also known as the fractional dust luminosity, was found to be correlated with the disk accretion activity (e.g. Kenyon & Hartmann 1995; Muzerolle et al. 2003). In particular, for mildly flared dusty disks, $L_{\rm dust}/L_\star \gtrsim$ 0.1–0.2 cannot be simply explained by dust reprocessing of stellar radiation alone (Kenyon & Hartmann 1995) but indicates that a significant amount of IR excesses may be contributed by self-radiation of an actively accreting disk, whereas YSOs with 0.001 $\lesssim L_{\rm dust}/L_\star \lesssim$ 0.1 are expected to be mostly evolved objects with weaker or no observable accretion activity (e.g. Cieza et al. 2007). Moreover, most gas-poor debris disks (systems which are dominated by second-generation dust produced by the collision of planetesimals) were found to have $L_{\rm dust}/L_\star$ well below 0.001 (e.g. Currie & Kenyon 2009; Eiroa et al. 2013; Matthews et al. 2014; Su et al. 2006; Trilling et al. 2008).

We determined $L_{\rm dust}$ as an integral of the R06 model SED of the circumstellar dust (disk+envelope) that best fits the emergent IR excess emission, and $L_\star$ as $(R_\star/R_\odot)^2(T_\star/T_\odot)^4$, where $R_\star$ and $T_\star$ are the stellar radius and effective temperature, respectively. The distribution of YSOs from different Stages on the $L_{\rm dust}/L_\star$ vs. $\lambda_{\rm turnoff}$ diagram is shown in Figure 10. The Stage I and III YSOs are well separated at $L_{\rm dust}/L_\star \sim$ 0.1, whereas the Stage II YSOs have a range of $L_{\rm dust}/L_\star$ from $\sim$ 0.01 to 1. Moreover, there is a general trend that the median $L_{\rm dust}/L_\star$ decreases with increasing $\lambda_{\rm turnoff}$ for YSOs at different evolutionary stages, pointing to an inside-out disk clearing process for at least the small dust grains.

5.3 Disk Inner Radius vs. $\alpha_{\rm excess}$

The inner radius of a dusty disk determines the highest temperature of dust grains orbiting around the central stellar source (e.g. Backman & Paresce 1993), and thus can affect $\alpha_{\rm excess}$. Figure 11 shows the relation between $\alpha_{\rm excess}$ and $R_{\rm in}/R_{\rm sub}$ with different $\lambda_{\rm turnoff}$, where $R_{\rm in}$ is the inner radius of the disk, and $R_{\rm sub}$ is the dust sublimation radius by assuming a sublimation temperature of 1600 K (R06). The bottom right panel of Figure 11 shows the corresponding distribution for the full sample.

There is a positive correlation between $R_{\rm in}/R_{\rm sub}$ and $\alpha_{\rm excess}$ at $R_{\rm in}/R_{\rm sub} \gtrsim$ 10 and $\alpha_{\rm excess}$ $\gtrsim$ 0.0, irrespective of $L_{\rm dust}/L_\star$ and $\lambda_{\rm turnoff}$. A similar trend (not shown in the paper) also exists between $R_{\rm in}$ and $\alpha_{\rm excess}$ at $R_{\rm in} >$ 0.5 AU and $\alpha_{\rm excess} \gtrsim 0.0$. We note that a positive correlation was also found between disk inner radii (or hole radii) and disk masses for 35 c2d YSOs by Merín et al. (2010).

5.4 Disk Flaring vs. $\alpha_{\rm excess}$

Compared to a completely flat disk geometry, a flaring geometry increases the disk area that intercepts stellar radiation at large radii, and thus enhances the mid- to far-IR emission (e.g. Kenyon & Hartmann 1987; Chiang & Goldreich 1997). The disk flaring power β describes the radial gradient of the disk scale height h, i.e. $h(r) \propto r^\beta$, where r is the cylindrical radius along the disk. The relationship between β and $\alpha_{\rm excess}$ for our YSOs is shown in Figure 12. While no significant correlation between β and $\alpha_{\rm excess}$ was found for the overall sample, a majority of the disks with $\alpha_{\rm excess}$ $<$ 0.0 follow a trend that $\alpha_{\rm excess}$ increases with β, suggesting that the lack of a correlation between $R_{\rm in}/R_{\rm sub}$ and $\alpha_{\rm excess}$ for disks with $R_{\rm in}/R_{\rm sub} \lesssim 1$ can be in part attributed to the disk flaring.

5.5 Discussion

A variety of physical mechanisms have been invoked to explain the circumstellar disk evolution and clearing processes (e.g. Henning & Meeus 2011; Williams & Cieza 2011). The few commonly-considered mechanisms include viscous disk accretion (e.g. Hartmann et al. 1998; Lynden-Bell & Pringle 1974; Shakura & Sunyaev 1973), grain growth and dust settling (e.g. Dullemond & Dominik 2005; Tanaka et al. 2005), photoevaporative dispersal (e.g. Alexander et al. 2006a,b; Gorti & Hollenbach 2009; Hollenbach et al. 1994; Shu et al. 1993) and dynamical clearing by companion stars or planets (e.g. Artymowicz & Lubow 1994; Kley & Nelson 2012; Lubow & D'Angelo 2006; Zhu et al. 2012). While all of these proposed processes may operate simultaneously, it is important to probe the dominant process(es) at different stages of disk evolution.

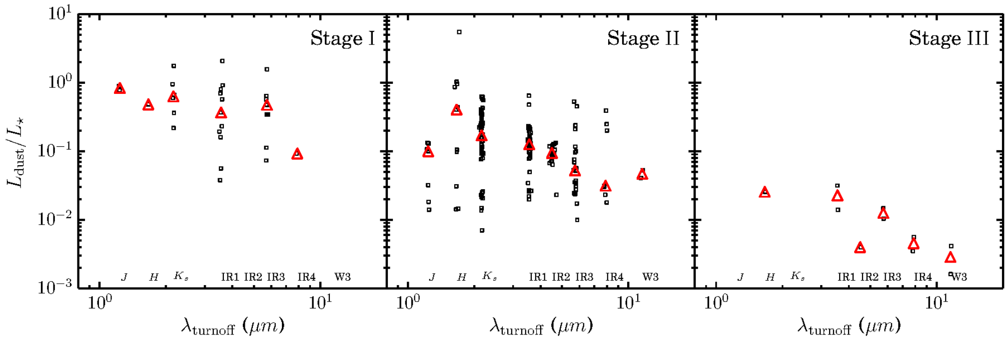

Fig. 10 Distributions of the fractional dust luminosity $L_{\rm dust}/L_\star$ vs. $\lambda_{\rm turnoff}$. YSOs at different evolutionary stages are plotted separately in different panels. The median $L_{\rm dust}/L_\star$ at different $\lambda_{\rm turnoff}$ is represented as red triangles.

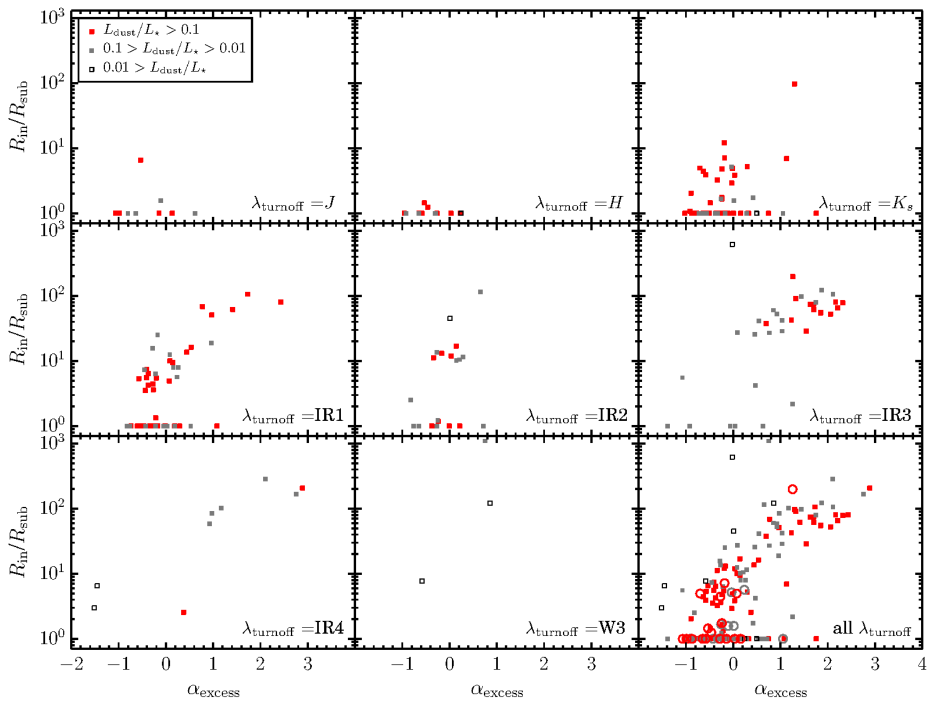

Fig. 11 Distribution of disk inner radius $R_{\rm in}$ vs. $\alpha_{\rm excess}$ for different $\lambda_{\rm turnoff}$. $R_{\rm in}$ is normalized by the dust sublimation radius $R_{\rm sub}$. YSOs with different ranges of $L_{\rm dust}/L_\star$ are plotted with different symbols, as indicated in the top left panel. The distribution for the full sample is shown in the bottom right panel, where objects with 70 µm detections are shown as red open circles.

5.5.1 From $\alpha_{\rm excess}$ to disk geometry

The near- to mid-IR $\alpha_{\rm excess}$ is primarily affected by clearing of the inner disk and flaring of the outer disk. In particular, the edge region of the optically thick inner disk, which is determined by either

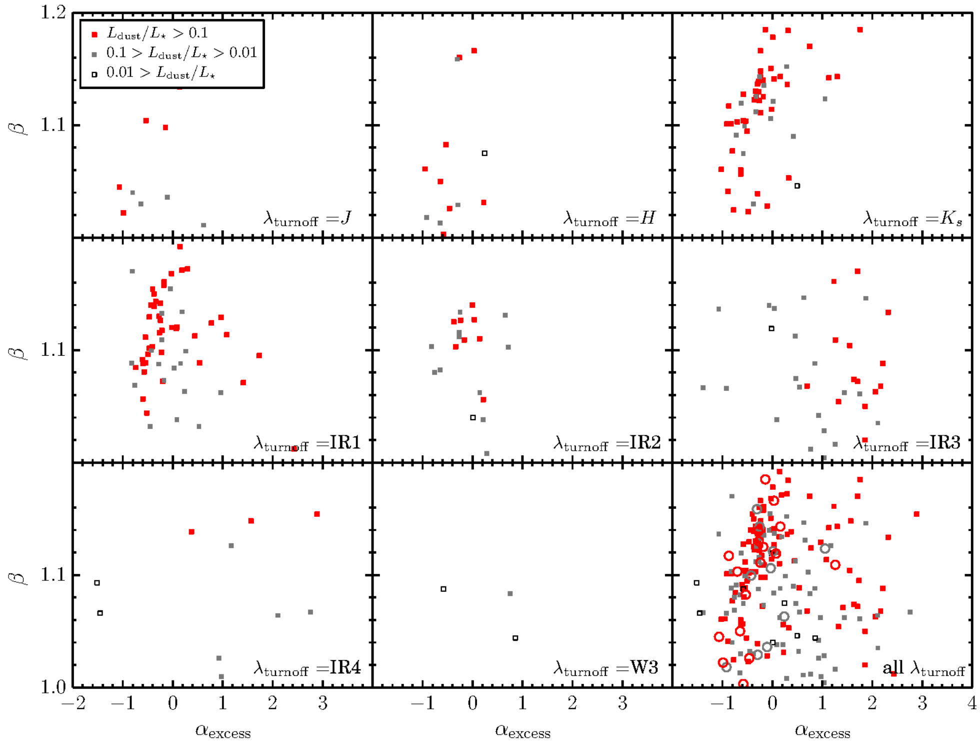

Fig. 12 Distribution of disk flaring power β vs. $\alpha_{\rm excess}$ for different $\lambda_{\rm turnoff}$. As displayed in Fig. 11, YSOs with different ranges of $L_{\rm dust}/L_\star$ are plotted with different symbols, as indicated in the top left panel. Distribution of the full sample is shown in the bottom right panel, where objects with 70 μm detections are shown as red open circles.

dust sublimation or some clearing processes, is directly illuminated by stellar irradiation and thus contributes most to the excess emission of hot dust, with the irradiation peak of this inner edge being shifted from near- to mid-IR as the disk is progressively cleared inside-out. In addition, as the disk evolves, dust settling or other clearing processes may result in a gradual reduction of disk flaring, which would in turn reduce the disk area that intercepts stellar radiation and thus suppresss the reprocessed cooler dust emission. Therefore, a progressively increasing disk inner edge is expected to increase $\alpha_{\rm excess}$, whereas a smaller flaring power in the outer disk can result in a smaller $\alpha_{\rm excess}$.

Our results suggest that variation of $\alpha_{\rm excess}$ above ~ 0.0 primarily reflects the variation of disk clearing radii, whereas variation of $\alpha_{\rm excess}$ below ~ 0.0 is largely related to a variation in the disk flaring power. Disk flaring is only important in shaping the near to mid-IR SEDs when $R_{\rm in} \lesssim 10 \times R_{\rm sub}$ (> 0.5 AU for our sample). The lack of correlation between $\alpha_{\rm excess}$ and disk flaring power at $R_{\rm in} \gtrsim 10 \times R_{\rm sub}$ implies that either the outer disk geometry does not vary synchronously with the inside-out disk clearing processes or spectral slopes at $\lambda \lesssim 24$ μm are not sensitive to the outer disk flaring. The small sample size of our disks (especially those with $\alpha_{\rm excess} > 0.0$) with detection at 70 μm, which is more sensitive to the outer disk flaring than shorter wavelengths (e.g. Sicilia-Aguilar et al. 2015), makes it hard to ascertain whether or not the outer disk flaring decreases or increases as the disk is cleared from the inside out. Recent studies of transitional disks in several nearby star-forming regions by Howard et al. (2013) and Keane et al. (2014) found that the continuum normalized [O I]

63.18 μm line luminosities, which trace the cool, outer disks, are suppressed by a factor of ~ 2 on average with respect to the classical full disks, and this suppression was attributed to reduction of either the outer disk flaring or gas-to-dust ratio.

5.5.2 Probing Disk Dispersal Processes with Transitional Disks

There may be a variety of evolutionary paths from the optically thick full disks to optically thin to debris disks. Distinguishing different disk dispersal processes is crucial for understanding how the planetary systems formed from protoplanetary disks. The partially-cleared transitional disks, which have little or no excess emission in the near-IR ($\lesssim 5$ μm) and thus in optically thin inner opacity holes but have a significant excess at longer wavelengths (e.g. Brown et al. 2007; Calvet et al. 2005; Strom et al. 1989; Skrutskie et al. 1990), provide a unique opportunity to probe different disk clearing mechanisms because different mechanisms are expected to result in very different IR spectral slopes, disk luminosities, and accretion activities in the short transitional stages (e.g. Alexander et al. 2014; Cieza et al. 2010; Najita et al. 2007).

To open an inner opacity hole through photoevaporation, the disk viscous accretion rate has to fall below the photoevaporation rate (e.g. Alexander et al. 2006a; Owen et al. 2010), and once this happens, the full disks, composed of gas and dust grains, can be quickly dissipated from the inside out in $\lesssim$ 0.1 Myr which is an order of magnitude shorter than the typical lifetime of a disk. Besides a low fractional disk luminosity and steep IR spectral slope (e.g. $\alpha_{\rm excess} < 0.0$), another important consequence from photoevaporative clearing is that little or no accretion is expected once an inner hole is opened. In contrast, dynamical clearing by giant planets may sustain a small but still considerable amount of disk accretion across the inner opacity hole and relatively high outer disk masses and luminosities, and thus raising mid- to far-IR SEDs (e.g. Alexander 2008; Najita et al. 2007). Different from both photoevaporation and dynamical clearing, the pure grain growth and dust settling processes can result in an efficient depletion of small grains (and thus suppression of near- to mid-IR emission) from the inside out over time scales much smaller than 0.1 Myr (e.g. Dullemond & Dominik 2005), with little direct influence on accretion activity.

All of our YSOs have $L_{\rm dust}/L_\star > 10^{-3}$, and 49 (23%) have $\lambda_{\rm turnoff} \geq$ IR3 and thus can be classified as transitional disks. Recall that our sample disks with $\lambda_{\rm turnoff} \geq$ IR3 exhibit a remarkably higher median and larger scatter of $\alpha_{\rm excess}$ than those with $\lambda_{\rm turnoff} <$ IR3 (Fig. 9). The fraction of transitional disks in our sample is slightly higher yet still comparable to previous studies of nearby star clusters or star-forming regions (e.g. Currie & Kenyon 2009; Dahm & Carpenter 2009; Fang et al. 2009; Hernández et al. 2007b; Kim et al. 2009; Lada et al. 2006). The distribution of our sample on the $\alpha_{\rm excess}$ vs. $L_{\rm dust}/L_\star$ plane is shown in Figure 13, where the transitional disks are plotted as black squares (*filled* for those with $T_\star < 4000$ K, and *open* for those with $T_\star > 4000$ K). Note that previous studies did not subtract the stellar photosphere emission when calculating the excess spectral index, which tends to underestimate the "genuine" $\alpha_{\rm excess}$.

As is shown in Figure 13, the majority of the disks with $\lambda_{\rm turnoff} <$ IR3 are clustered toward the upper left corner, with $L_{\rm dust}/L_\star \gtrsim 10^{-1}$ and $\alpha_{\rm excess} \lesssim$ 0.0, whereas the disks with $\lambda_{\rm turnoff} \geq$ IR3 seem to follow a sequence from the upper right to the lower left, with none of them having $L_{\rm dust}/L_\star > 10^{-1}$ and $\alpha_{\rm excess} <$ 0.0. Most of the objects around the upper left corner are expected to have accreting full disks, and they are clearly separated from the population of transitional disks in Figure 13. A similar separation of transitional disks and full disks was also recently found by Sicilia-Aguilar et al. (2015) based on the relation between spectral indices and accretion rates. Among the objects with $\lambda_{\rm turnoff} <$ IR3, 14 (7%) have $\alpha_{\rm excess} <$ 0.0 and $L_{\rm dust}/L_\star \leq$ 0.003. These 7% of objects are consistent with being the so-called "anemic" (e.g. Lada et al. 2006) or "homologously depleted" (e.g. Currie & Sicilia-Aguilar 2011) disks, which have detectable excess emission that decreases steadily at all wavelengths.

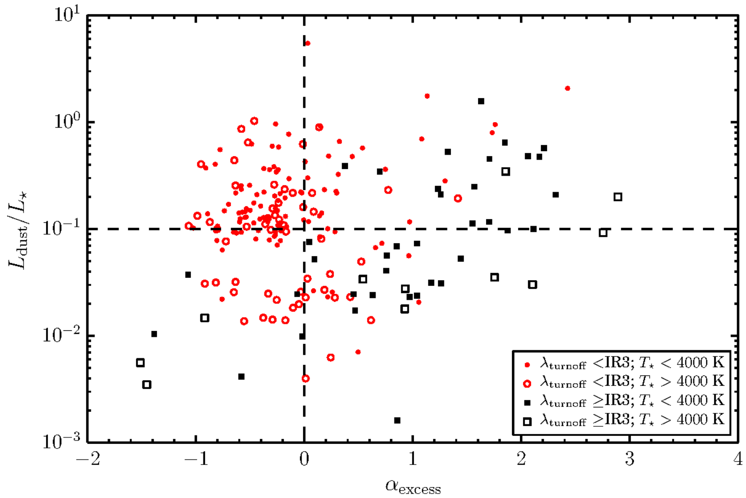

Fig. 13 $\alpha_{\rm excess}$ is plotted against the fractional disk luminosities $L_{\rm dust}/L_\star$. Disks with $\lambda_{\rm turnoff} <$ and $\geq$ IR3 (transitional disks) are plotted as red open circles and black filled squares respectively. The horizontal dashed line separates the sample into disks with $L_{\rm dust}/L_\star >$ and $<$ 0.1, and the vertical dashed line separates the sample into disks with $\alpha_{\rm excess} >$ and < 0.0. Most accreting disks were found to have $L_{\rm dust}/L_\star \geq$0.1. Transitional disks in the lower left part may be primarily cleared by photoevaporation, while those in the upper right part may be dynamically cleared by giant planets.

Transitional disks toward the lower left corner of Figure 13 may be more evolved than those toward the upper right. Among the 49 transitional disks, 41 (84%) have $\alpha_{\rm excess} > 0.0$ and 8 (16%) have $\alpha_{\rm excess} < 0.0$. Observations of UV continuum or recombination emission lines for all of our sample will be necessary for obtaining an ongoing disk accretion rate. The accretion activities are known to be closely connected to the disk's global properties, such as disk luminosities, masses and dust settling. If we instead use $L_{\rm dust}/L_\star$ to approximately discriminate disks with or without accretion activity at a dividing value = 0.1, 17 (35%) of the 49 transitional disks have $\alpha_{\rm excess} > 0.0$ and $L_{\rm dust}/L_\star > 0.1$, which may indicate the possibility of dynamical clearing by giant planets; Among the 32 (65%) disks with $L_{\rm dust}/L_\star < 0.1$, 8 have $\alpha_{\rm excess} < 0.0$ and 24 have $\alpha_{\rm excess} > 0.0$. The low $L_{\rm dust}/L_\star$ probably indicates that these 32 disks are primarily cleared by photoevaporation. None of our transitional disks have $\alpha_{\rm excess} < 0.0$ and $L_{\rm dust}/L_\star > 0.1$, so grain growth and dust settling alone are probably not important hole-opening mechanisms (Cieza et al. 2010). Furthermore, our finding that the median $\alpha_{\rm excess}$ of Stages I and II YSOs tends to increase with $\lambda_{\rm turnoff}$ also suggests that disk clearing is not primarily driven by grain growth which would otherwise result in a negative correlation between $\alpha_{\rm excess}$ and $\lambda_{\rm turnoff}$ (e.g. Dullemond & Dominik 2005).

6 SUMMARY

We have statistically explored the properties of the central stellar sources, the evolutionary stages, and the circumstellar disks for a sample of 211 Perseus YSOs by modeling the optical to mid-IR broadband SEDs with the R06 YSO evolution models. The median central stellar mass and age for the Perseus YSOs are ∼0.3 $M_\odot$ and ∼3.1 Myr respectively based on the Siess et al. (2000) PMS evolutionary models. About 81% of our sample are classified as Stage II objects which are characterized by having optically thick disks, ∼ 14% are classified as Stage I objects which are characterized by having significant infalling envelopes, and the remaining 5% are classified as Stage III objects with optically thin disks. Our primary results are summarized as follows.

(1) The evolutionary Stages as determined from the SED modeling have a general correspondence with the traditional classes that are based on spectral indices. In particular, $\sim$ 90% of the Class II YSOs fall into the Stage II phase which is characterized by optically thick disks, and 75% of the Class I YSOs fall into the Stage I phase which is characterized by significant infalling envelopes. Nevertheless, relating the Class III and FLAT YSOs to specific evolutionary stages is uncertain. In particular, half of the Class III YSOs fall into Stage II and the other half fall into the optically thin Stage III phase, and half of the Class FLAT YSOs fall into Stage I and the other half fall into the Stage II phase.

(2) We determined the turnoff wave band ($\lambda_{\rm turnoff}$) longward of which significant IR excesses with respect to the stellar photosphere level start to be observed and the excess spectral indices $\alpha_{\rm excess}$ at $\lambda > \lambda_{\rm turnoff}$. The median and standard deviation of $\alpha_{\rm excess}$ for the Stage I and Stage II YSOs tend to increase with $\lambda_{\rm turnoff}$, especially at $\lambda_{\rm turnoff} \geq$ IRAC 5.8 μm. There is a general trend that the median fractional dust luminosity $L_{\rm dust}/L_\star$ decreases with increasing $\lambda_{\rm turnoff}$, pointing to an inside-out disk clearing process of small dust grains. We found a positive correlation between $\alpha_{\rm excess}$ and disk inner radius $R_{\rm in}$, and a lack of correlation between $\alpha_{\rm excess}$ and disk flaring at $\alpha_{\rm excess} \gtrsim 0.0$ and $R_{\rm in} \gtrsim 10{\times}R_{\rm sub}$, which indicates that, first, the near- to mid-IR spectral slopes primarily reflect the progressive disk clearing from the inside out once $R_{\rm in} \gtrsim 10{\times}R_{\rm sub}$; second, the outer disk flaring either does not vary synchronously with the inner disk clearing processes or has little appreciable influence on the spectral slopes at wavelengths $\lesssim$24 μm.

(3) About 23% (49) of our YSOs are classified as transitional disks, which have $\lambda_{\rm turnoff} \geq$ IRAC 5.8 μm and $L_{\rm dust}/L_\star > 10^{-3}$. By using the $L_{\rm dust}/L_\star$ to approximately discriminate disks with or without accretion activity at a dividing value of 0.1, 35% of the transitional disks have $\alpha_{\rm excess} > 0.0$ and $L_{\rm dust}/L_\star > 0.1$, implying the possibility of dynamical clearing by giant planets; 65% have $L_{\rm dust}/L_\star < 0.1$, which is consistent with the expectation of photoevaporative clearing; None of our disks have $\alpha_{\rm excess} < 0.0$ or $L_{\rm dust}/L_\star > 0.1$, so grain growth and dust settling are probably not the driving mechanisms in disk clearing, in line with the trend that the median $\alpha_{\rm excess}$ increases, rather than decreases, with $\lambda_{\rm turnoff}$.

An indispensable diagnostic for the evolutionary stages of YSOs and their circumstellar disks is the current accretion rate, which is usually determined either from recombination lines or ultraviolet continuum excesses. Different disk clearing processes can lead to different disk accretion properties, the effect of which is especially prominent in transitional stages. Moreover, similar to many previous studies, our current work is heavily biased against Stage III YSOs with optically thin or anemic disks. To understand the disk evolution and dispersal processes, a systematic census of Stage III YSOs and their disk accretion activity is imperative. Therefore, our future direction will include 1) a systematic spectroscopic followup of our YSOs with the Large Sky Area Multi-Object Fiber Spectroscopic Telescope (LAMOST; Cui et al. 2012) to place stringent constraints on the ongoing accretion activity; 2) wide-field time-series optical photometry across the whole Perseus region for an unbiased census of Stage III disks with the PMO Xuyi 1.2-m Schmidt Telescope, in order to further probe the dominant disk dispersal mechanisms.

Acknowledgements We thank the anonymous referee for his/her helpful comments that improved this manuscript. We acknowledge the support of the National Natural Science Foundation of China (NSFC, Grant No. 11390373). HXZ acknowledges support from the China Postdoctoral Science Foundation (Grant No. 2013M530008), and the CAS-CONICYT Postdoctoral Fellowship, administered by the Chinese Academy of Sciences South America Center for Astronomy (CASSACA). MF acknowledges the NSFC (Grant No. 11203081).

References

Alexander, R. 2008, New Astron. Rev., 52, 60
Alexander, R. D., Clarke, C. J., & Pringle, J. E. 2006a, MNRAS, 369, 216
Alexander, R. D., Clarke, C. J., & Pringle, J. E. 2006b, MNRAS, 369, 229
Alexander, R., Pascucci, I., Andrews, S., Armitage, P., & Cieza, L. 2014, Protostars and Planets VI, 475
Allen, L. E., Calvet, N., D'Alessio, P., et al. 2004, ApJS, 154, 363
Andersen, M., Meyer, M. R., Greissl, J., & Aversa, A. 2008, ApJ, 683, L183
Andre, P., Ward-Thompson, D., & Barsony, M. 1993, ApJ, 406, 122
Andrews, S. M., & Williams, J. P. 2005, ApJ, 631, 1134
Artymowicz, P., & Lubow, S. H. 1994, ApJ, 421, 651
Backman, D. E., & Paresce, F. 1993, in Protostars and Planets III, ed. E. H. Levy & J. I. Lunine, 1253
Bally, J., Walawender, J., Johnstone, D., Kirk, H., & Goodman, A. 2008, The Perseus Cloud, ed. B. Reipurth, Handbook of Star Forming Regions, Volume I (The Northern Sky ASP Monograph Publications), 308
Baraffe, I., Chabrier, G., Allard, F., & Hauschildt, P. H. 1998, A&A, 337, 403
Beckwith, S. V. W., Sargent, A. I., Chini, R. S., & Guesten, R. 1990, AJ, 99, 924
Belikov, A. N., Kharchenko, N. V., Piskunov, A. E., Schilbach, E., & Scholz, R.-D. 2002, A&A, 387, 117
Bernasconi, P. A., & Maeder, A. 1996, A&A, 307, 829
Brown, J. M., Blake, G. A., Dullemond, C. P., et al. 2007, ApJ, 664, L107
Calvet, N., Briceño, C., Hernández, J., et al. 2005, AJ, 129, 935
Calvet, N., D'Alessio, P., Hartmann, L., et al. 2002, ApJ, 568, 1008
Chen, B.-Q., Liu, X.-W., Yuan, H.-B., Huang, Y., & Xiang, M.-S. 2015, MNRAS, 448, 2187
Chen, B.-Q., Liu, X.-W., Yuan, H.-B., et al. 2014, MNRAS, 443, 1192
Chiang, E. I., & Goldreich, P. 1997, ApJ, 490, 368
Cieza, L., Padgett, D. L., Stapelfeldt, K. R., et al. 2007, ApJ, 667, 308
Cieza, L. A., Schreiber, M. R., Romero, G. A., et al. 2010, ApJ, 712, 925
Cui, X.-Q., Zhao, Y.-H., Chu, Y.-Q., et al. 2012, RAA (Research in Astronomy and Astrophysics), 12, 1197
Currie, T., & Kenyon, S. J. 2009, AJ, 138, 703
Currie, T., & Sicilia-Aguilar, A. 2011, ApJ, 732, 24
Dahm, S. E., & Carpenter, J. M. 2009, AJ, 137, 4024
D'Antona, F., & Mazzitelli, I. 1997, Mem. Soc. Astron. Italiana, 68, 807
de Zeeuw, P. T., Hoogerwerf, R., de Bruijne, J. H. J., Brown, A. G. A., & Blaauw, A. 1999, AJ, 117, 354
Dotter, A., Chaboyer, B., Jevremović, D., et al. 2008, ApJS, 178, 89
Dullemond, C. P., & Dominik, C. 2005, A&A, 434, 971
Dullemond, C. P., Hollenbach, D., Kamp, I., & D'Alessio, P. 2007, Protostars and Planets V, 555
Eiroa, C., Marshall, J. P., Mora, A., et al. 2013, A&A, 555, A11
Enoch, M. L., Young, K. E., Glenn, J., et al. 2006, ApJ, 638, 293
Espaillat, C., Ingleby, L., Furlan, E., et al. 2013, ApJ, 762, 62
Evans, II, N. J., Allen, L. E., Blake, G. A., et al. 2003, PASP, 115, 965
Evans, II, N. J., Dunham, M. M., Jørgensen, J. K., et al. 2009, ApJS, 181, 321
Fang, M., van Boekel, R., Wang, W., et al. 2009, A&A, 504, 461
Fang, M., Kim, J. S., van Boekel, R., et al. 2013, ApJS, 207, 5
Fitzpatrick, E. L. 1999, PASP, 111, 63
Goodman, A. A., Alves, J. F., Arce, H. G., et al. 2005, in Bulletin of the American Astronomical Society, 37, American Astronomical Society Meeting Abstracts, #184.20
Gorti, U., & Hollenbach, D. 2009, ApJ, 690, 1539
Greene, T. P., Wilking, B. A., Andre, P., Young, E. T., & Lada, C. J. 1994, ApJ, 434, 614
Greissl, J., Meyer, M. R., Wilking, B. A., et al. 2007, AJ, 133, 1321

Hartmann, L., Calvet, N., Gullbring, E., & D'Alessio, P. 1998, ApJ, 495, 385
Harvey, P., Merín, B., Huard, T. L., et al. 2007, ApJ, 663, 1149
Hatchell, J., Richer, J. S., Fuller, G. A., et al. 2005, A&A, 440, 151
Henning, T., & Meeus, G. 2011, Physical Processes in Circumstellar Disks around Young Stars, ed. P. J. V. Garcia, 114
Herbig, G. H. 1998, ApJ, 497, 736
Hernández, J., Hartmann, L., Megeath, T., et al. 2007a, ApJ, 662, 1067
Hernández, J., Calvet, N., Briceño, C., et al. 2007b, ApJ, 671, 1784
Hillenbrand, L. A., Bauermeister, A., & White, R. J. 2008, in Astronomical Society of the Pacific Conference Series, 384, 14th Cambridge Workshop on Cool Stars, Stellar Systems, and the Sun, ed. G. van Belle, 200
Hillenbrand, L. A., & Carpenter, J. M. 2000, ApJ, 540, 236
Hollenbach, D., Johnstone, D., Lizano, S., & Shu, F. 1994, ApJ, 428, 654
Howard, C. D., Sandell, G., Vacca, W. D., et al. 2013, ApJ, 776, 21
Hsieh, T.-H., & Lai, S.-P. 2013, ApJS, 205, 5
Hughes, A. M., Andrews, S. M., Wilner, D. J., et al. 2010, AJ, 140, 887
Jørgensen, J. K., Johnstone, D., Kirk, H., & Myers, P. C. 2007, ApJ, 656, 293
Keane, J. T., Pascucci, I., Espaillat, C., et al. 2014, ApJ, 787, 153
Kenyon, S. J., & Hartmann, L. 1987, ApJ, 323, 714
Kenyon, S. J., & Hartmann, L. 1995, ApJS, 101, 117
Kim, K. H., Watson, D. M., Manoj, P., et al. 2009, ApJ, 700, 1017
Kley, W., & Nelson, R. P. 2012, ARA&A, 50, 211
Lada, C. J. 1987, in IAU Symposium, Vol. 115, Star Forming Regions, eds. M. Peimbert, & J. Jugaku, 1
Lada, C. J., Muench, A. A., Luhman, K. L., et al. 2006, AJ, 131, 1574
Levine, J. L., Steinhauer, A., Elston, R. J., & Lada, E. A. 2006, ApJ, 646, 1215
Liu, X.-W., Yuan, H.-B., Huo, Z.-Y., et al. 2014, in IAU Symposium, 298, eds. S. Feltzing, G. Zhao, N. A. Walton, & P. Whitelock, 310
Liu, X. W., Zhao, G., & Hou, J. L. 2015, RAA (Research in Astronomy and Astrophysics), 15, 1089
Lubow, S. H., & D'Angelo, G. 2006, ApJ, 641, 526
Lucas, P. W., Roche, P. F., & Tamura, M. 2005, MNRAS, 361, 211
Luhman, K. L., Rieke, G. H., Young, E. T., et al. 2000, ApJ, 540, 1016
Luhman, K. L., Briceño, C., Stauffer, J. R., et al. 2003a, ApJ, 590, 348
Luhman, K. L., Stauffer, J. R., Muench, A. A., et al. 2003b, ApJ, 593, 1093
Luhman, K. L. 2007, ApJS, 173, 104
Luhman, K. L., Allen, P. R., Espaillat, C., Hartmann, L., & Calvet, N. 2010, ApJS, 186, 111
Lupton, R. 2005, Transformations between SDSS magnitudes and $UBVR_cI_c$, *http://www.sdss.org/dr5/ algorithms/sdssUBVRITransform.html*
Lynden-Bell, D., & Pringle, J. E. 1974, MNRAS, 168, 603
Matthews, B., Kennedy, G., Sibthorpe, B., et al. 2014, ApJ, 780, 97
Merín, B., Jørgensen, J., Spezzi, L., et al. 2008, ApJS, 177, 551
Merín, B., Brown, J. M., Oliveira, I., et al. 2010, ApJ, 718, 1200
Moraux, E., Bouvier, J., Stauffer, J. R., & Cuillandre, J.-C. 2003, A&A, 400, 891
Muench, A. A., Lada, E. A., Lada, C. J., & Alves, J. 2002, ApJ, 573, 366
Muench, A. A., Lada, E. A., Lada, C. J., et al. 2003, AJ, 125, 2029
Muench, A. A., Lada, C. J., Luhman, K. L., Muzerolle, J., & Young, E. 2007, AJ, 134, 411
Muzerolle, J., Calvet, N., Hartmann, L., & D'Alessio, P. 2003, ApJ, 597, L149
Muzerolle, J., Adame, L., D'Alessio, P., et al. 2006, ApJ, 643, 1003
Najita, J. R., Strom, S. E., & Muzerolle, J. 2007, MNRAS, 378, 369
Owen, J. E., Ercolano, B., Clarke, C. J., & Alexander, R. D. 2010, MNRAS, 401, 1415

Palla, F., & Stahler, S. W. 1999, ApJ, 525, 772
Povich, M. S., Kuhn, M. A., Getman, K. V., et al. 2013, ApJS, 209, 31
Rice, W. K. M., Wood, K., Armitage, P. J., Whitney, B. A., & Bjorkman, J. E. 2003, MNRAS, 342, 79
Ridge, N. A., Di Francesco, J., Kirk, H., et al. 2006, AJ, 131, 2921
Robitaille, T. P., Whitney, B. A., Indebetouw, R., Wood, K., & Denzmore, P. 2006, ApJS, 167, 256
Robitaille, T. P., Whitney, B. A., Indebetouw, R., & Wood, K. 2007, ApJS, 169, 328
Robitaille, T. P. 2008, in Astronomical Society of the Pacific Conference Series, 387, Massive Star Formation: Observations Confront Theory, eds. H. Beuther, H. Linz, & T. Henning, 290
Roeser, S., Demleitner, M., & Schilbach, E. 2010, AJ, 139, 2440
Salpeter, E. E. 1955, ApJ, 121, 161
Scholz, A., Geers, V., Jayawardhana, R., et al. 2009, ApJ, 702, 805
Shakura, N. I., & Sunyaev, R. A. 1973, A&A, 24, 337
Shu, F. H., Johnstone, D., & Hollenbach, D. 1993, Icarus, 106, 92
Sicilia-Aguilar, A., Hartmann, L., Calvet, N., et al. 2006, ApJ, 638, 897
Sicilia-Aguilar, A., Roccatagliata, V., Getman, K., et al. 2015, A&A, 573, A19
Siess, L., Dufour, E., & Forestini, M. 2000, A&A, 358, 593
Skrutskie, M. F., Dutkevitch, D., Strom, S. E., et al. 1990, AJ, 99, 1187
Slesnick, C. L., Hillenbrand, L. A., & Carpenter, J. M. 2004, ApJ, 610, 1045
Strom, S. E., Strom, K. A., & Carrasco, L. 1974, PASP, 86, 798
Strom, K. M., Strom, S. E., Edwards, S., Cabrit, S., & Skrutskie, M. F. 1989, AJ, 97, 1451
Su, K. Y. L., Rieke, G. H., Stansberry, J. A., et al. 2006, ApJ, 653, 675
Surace, J. A., Sanders, D. B., & Mazzarella, J. M. 2004, AJ, 127, 3235
Swenson, F. J., Faulkner, J., Rogers, F. J., & Iglesias, C. A. 1994, ApJ, 425, 286
Tanaka, H., Himeno, Y., & Ida, S. 2005, ApJ, 625, 414
Trilling, D. E., Bryden, G., Beichman, C. A., et al. 2008, ApJ, 674, 1086
Weights, D. J., Lucas, P. W., Roche, P. F., Pinfield, D. J., & Riddick, F. 2009, MNRAS, 392, 817
Wilking, B. A., Meyer, M. R., Greene, T. P., Mikhail, A., & Carlson, G. 2004, AJ, 127, 1131
Williams, J. P., & Cieza, L. A. 2011, ARA&A, 49, 67
Winston, E., Megeath, S. T., Wolk, S. J., et al. 2009, AJ, 137, 4777
Winston, E., Megeath, S. T., Wolk, S. J., et al. 2010, AJ, 140, 266
Yi, S. K., Kim, Y.-C., & Demarque, P. 2003, ApJS, 144, 259
Zhang, H.-H., Liu, X.-W., Yuan, H.-B., et al. 2013, RAA (Research in Astronomy and Astrophysics), 13, 490
Zhang, H.-H., Liu, X.-W., Yuan, H.-B., et al. 2014, RAA (Research in Astronomy and Astrophysics), 14, 456
Zhu, Z., Nelson, R. P., Dong, R., Espaillat, C., & Hartmann, L. 2012, ApJ, 755, 6